UNIVERSITY OF SOUTHAMPTON

FACULTY OF ENGINEERING, SCIENCE & MATHEMATICS

Aerodynamics and Flight Mechanics Group

Computational Study of Wing in Ground Effect Flows

by

Liam Paul O'Donnell

Thesis for the degree of Master of Philosophy

December 2004

Acknowledgements

I would firstly like to thank the University of Southampton for providing a grant to enable me to carry out this project. Thanks also to my supervisor Dr. Gary Coleman for his continued support in achieving this finished thesis. Thanks to all the guys in the department and everyone I met while in Southampton for making my time there so enjoyable. Most importantly, special thanks to my parents, brothers and girlfriend for their dedicated support and for prodding me numerous times in the right direction.

UNIVERSITY OF SOUTHAMPTON

ABSTRACT

FACULTY OF ENGINEERING, SCIENCE & MATHEMATICS
SCHOOL OF ENGINEERING SCIENCES

Master of Philosophy

COMPUTATIONAL STUDY OF WING IN GROUND EFFECT FLOWS

by Liam Paul O'Donnell

The performance of an aerofoil in ground effect has been studied using two computational packages, CFL3D and Fluent. Using these packages, the k-ε, k-ω, Shear Stress Transport and the Spalart-Allmaras model [17] were applied to the problem. Grid dependency was tested and the results were compared to experimental data. It was found that C-type grids performed best but caused problems in fully structured grids due to grid stretching issues. The level of grid sensitivity was investigated for all turbulence models over a range of ride heights. The Shear Stress Transport and Spalart-Allmaras models performed the best with the other two models providing poor accuracy. It is shown also that a compressible flow solver does not predict incompressible flow problems well, although some fixes can be implemented with a large time penalty. A two-dimensional computational database of wing in ground effect flows incorporating the aerofoil has been developed. This will be vital to produce further work, which will be greatly assisted by the inclusion of the Detached Eddy Simulation model in Fluent.

Contents

List of Figures

List of Tables

Nomenclature

C_P	-	Coefficient of Pressure
C_L	-	Coefficient of Lift
C_D	-	Coefficient of Drag
c	-	Chord Length
x	-	Grid Scale in x-direction
y	-	Grid Scale in y-direction
x/c	-	Non-Dimensional Grid Aerofoil length in x-direction
z/c	-	Non-Dimensional Grid Aerofoil length in z-direction
it	-	Number of Iterations
h	-	Height from the ground (lowest point of aerofoil to the ground)
h/c	-	Non-dimensionalised Ride Height
mm	-	millimetres
U_∞	-	Freestream Velocity
m/s	-	meters per second
CFL3D	-	Computational Fluid Laboratories 3 Dimensional
SST	-	Shear Stress Transport
SA	-	Spalart-Allmaras (turbulence model)
RANS	-	Reynolds-Averaged Navier Stokes
URANS	-	Unsteady Reynolds-Averaged Navier Stokes
LES	-	Large Eddy Simulations
DES	-	Detached Eddy Simulations
DNS	-	Direct Numerical Simulations
NACA	-	National Advisory Committee for Aeronautics
NASA	-	National Aeronautics and Space Administration
SGS	-	Sub Grid Scales
F1	-	Formula 1

Greek Symbols

α	-	Angle of Attack
ω_z	-	Vorticity in the Spanwise Direction

Chapter 1

Introduction and Literature Review

1.1 Introduction

The use of wings on cars, specifically racing cars, has been around since 1966. These early wings were fairly rudimentary and not very efficient, but showed enough of a gain in performance to become an important element of future racing car designs. The initial wings were mounted far from the ground at the front and rear of a car and were placed on tall struts [1]. For several reasons, including safety, these wings were banned for a short time. By 1970 they returned and were placed in the general configuration that is common-place today. The rear wing was attached close to the rear wheels and the front wing close to the ground ahead of the front wheels. This prompted a great deal of study on both wing configurations as both have a critical effect on racing car performance and driveability. This is exacerbated by the fact that the front wing of a modern racing car operates in very strong ground effect, meaning it operates in close proximity to the ground and its aerodynamic properties are affected by the ground [2]. These wings can produce up to 25-30% of the aerodynamic forces on the car [3]. However, these wings are not the only critical part on the car regarding aerodynamic performance. The entire body has a role to play, with particular emphasis on the rear wing and the undertray or diffuser. One very important aspect in regards to the front wing is the suspension, and thus the speed and braking of the car. The reaction of the suspension to these inputs has a large impact on the performance of the front wing. As the car accelerates, the front of the car lifts as the load on the front suspension is reduced, and therefore the wing is lifted out of ground effect and the downforce is reduced. This causes the front to appear lighter from the driver's prospective, which is referred to as understeer. Likewise, as the car brakes, the height of the wing is decreased, and so the downforce balance from the front to the rear is affected dramatically as the downforce on the front wing increases while that on the rear wing is reduced. Therefore, the front turns into a corner faster than the rear. This is referred to as oversteer. However, if the suspension is very soft, the front wing, under braking, can go

very close to the ground. This culminates in the downforce being greatly reduced due to being too close to the ground [9] (in future: Zerihan). This leads to the front becoming light and understeer occurs again so that the car will not make the apex or best entry and exit angles of the corner for maximum speed. This shows that a well balanced car is essential to the overall speed, as cornering speed is as important, if not more so in certain racing series, as straight line speed.

An additional issue with the front wing is the wake it produces. As it is basically the leading edge of the car itself, the wake from the front wing has a huge effect on the aerodynamic efficiency of the body, the diffuser, the radiator, the rear wing and also very importantly the wheels.

1.2 Motivation

One of the greatest driving forces in understanding a wing in ground effect is their practical application. The use of such configurations in the motor racing industry is extremely important with up to 30% of the downforce on a modern Formula 1 Racing car produced by the front wing. The reason this varies is due to the large number of designs of both cars and the wings themselves, but also in the requirements put on their performance. As car designs vary, so do their individual performances. This leads to the front wing being tailored to suit the chassis and the other components. For instance, the engine is not ultimately designed with the front wing in mind but the front wing is designed with consideration to its own performance and its impact on the remainder of the car.

As the wing can affect the handling dynamics of a racing car, particularly in cornering, the properties of a generic single-element wing in ground effect needs to be fully understood before that of more complex configurations. These handling problems not only affect performance but also have a very important role to play in the safety of the car. The front wing allows a racing car to corner at much greater speeds than would normally be accomplished and so the potential for a more severe accident is greater. Therefore, any failure in the performance of the wing or poor application of the wing can result in a driver inadvertently losing control of the car at potentially fatal speeds.

These factors combine to make the wing in ground phenomenon an area of study which has a great deal of potential. This is coupled with the fact that very little information has been released to the scientific community in general by the current specialists in this area, namely the Racing Car teams.

There currently exists very little data examining the effect of a wing in ground effect, and the majority of the available data is carried out on a wing with a stationary ground. However, as pointed out by Zerihan, stationary-ground studies [4, 5, 6] are of little value with respect to quantitative results due to different viscous effects. In the case of the stationary-ground the boundary-layer velocity is equal to zero, whereas the moving-ground boundary-layer velocity is set equal to the free-stream velocity. Results presented by Razenbach & Barlow [4, 5, 6] and Jasinski & Selig [7] only study the wing in close proximity to a stationary ground with limited analysis carried out on a moving ground. Knowles, Donahue & Finnis [8] and Zerihan carried out some of the rare studies using a moving ground. These together cover a multitude of aerofoil and wing combinations including multi-element geometries, varying ride heights and effects of three-dimensional wings. These studies were predominantly experimental with their computational work limited to panel methods (Knowles et al [8]) or a few Reynolds-Averaged Navier-Stokes (RANS) simulations [9].

Therefore there is a need to further examine the physics of a wing in ground effect, using proper, moving ground boundary conditions. We choose for this work to use computational methods, furthering the work initiated by Zerihan.

1.3 Aims and Approach

The aims of this research programme are to:

- Perform numerical simulations on a single wing in ground effect. Use of a single wing allows the study of the physics of wing in ground effect flows without additional complexities.

- Compare the results with experimental data for the same configuration. This entails modelling the same wing as used in the wind tunnel.

- Examine the flowfield physics of the wing in ground effect.

- Contrast the various computational models and modelling techniques such as grid generation.

- Obtain a two-dimensional benchmark which can be used to base future development upon.

1.4 Literature Review

1.4.1 Relevant Research

While a double element configuration will not be studied, previous work concerning this type of configuration is popular due to its direct application to racing car front wings. This double element work provides limited data that allows a basic interpretation of the physics of a wing in ground effect.

1.4.2 Thin Aerofoil Theory - Terminology and Definitions

An aerofoil is defined by first drawing a mean camber line. The straight line that joins the leading and trailing ends of the mean camber line is called the chord line and its length is given the symbol 'c' (fig.1).

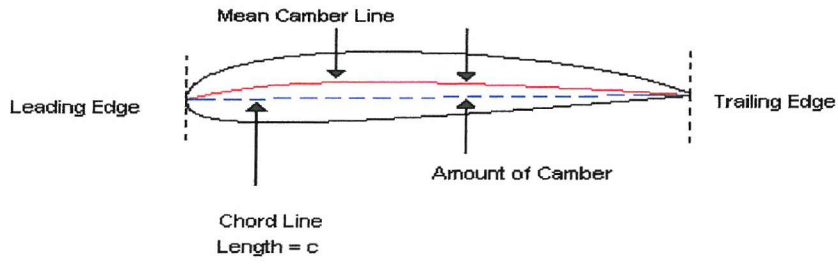

Figure 1. Aerofoil Geometry

To the mean camber line, a thickness distribution is added in a direction normal to the camber line to produce the final aerofoil shape. Equal amounts of thickness are added above and below the camber line. An aerofoil with no camber (i.e. a flat straight line for

camber) is a symmetric aerofoil. The angle that a freestream makes with the chord line is called the angle of attack.

1.4.3 Effect of the Ground on Aerodynamic Devices

The design of a wing was carried out initially with little or no thought given to the effect of the ground on the aerodynamic performance. Also significantly, up until recent years, little thought was given to the fact that the ground can be seen as moving relative to the wing. Experiments carried out incorporating the moving ground showed a marked difference to those carried out with a stationary ground. It was observed that in some cases the drag increased but in all cases the downforce increased [10]. This study was carried out on inverted wings.

Ground effect on wings has been widely studied using experimental techniques, but this research was mainly carried out on lift producing wings, and in each case the ground was stationary [11, 12, 13, 14]. The main problem with using a stationary ground is that the boundary layer will grow, but this can be removed to a certain extent using a stationary ground which starts a short distance upstream of the test section. Alternatively the boundary layer can be sucked away through the ground (Knowles et al [8]), but this can be a difficult and expensive technique. In any case using a stationary ground as opposed to a moving or rolling road section in a wind tunnel produces very different physics, even when the boundary layers are the same thickness. Therefore, as mentioned above, the only accurate way of modelling the effect experimentally is to use a rolling road wind tunnel. This was first successfully achieved by Klemin in the 1930's [15].

1.4.4 Up-Lifting Wings in Ground Effect

In order to comprehensively study a wing in ground effect, the topic of both downforce producing and lift producing wings must be assessed.

In early studies (e.g. [11]) pilots described a cushioning effect felt when flying close to the ground and that for given angles of attack, the lift increases and drag decreases. It was also observed that aircraft with high-lift wings and flap gears found it difficult to land and that when travelling nearly parallel to the ground the aircraft stays airborne for an unexpectedly

long time. This study also used a reflection method and showed that a liftslope increase can also be expected. Pressure distributions show that in proximity to the ground, the pressure on the pressure-surface (lower) increases, due to the image beneath the ground plane inducing a lower velocity in the region between the wing and the ground.
As commented by Zerihan, it is common for the lift at a given angle to increase, but it does not always lead to a corresponding increase in the maximum lift coefficient due to a reduction in the stalling angle being observed. Results appear to depend on the exact wing configuration, the representation of the ground plane boundary layer along with the aspect ratio of the wing. However, where the image aerofoil induces greater pressure on the pressure surface, the diffuser effect (separation at the trailing edge due to the close proximity of the trailing edges of the real and image wing) can cause a decrease in the pressure on the pressure surface.

1.4.5 Downforce-Producing Wings in Ground Effect

Experiments carried out by Knowles et al [8], described that when the aerofoil is in close proximity to the ground, there is an increase in the lift curve slope, the drag and the pitching moment. They also showed that all of these effects were non-linear, with the sharpest increases occurring between the area of ride-height/chord = 0.24 and 0.12 [10]. The explanation for the increase in downforce close to the ground is because of the interaction between the aerofoil and its image. This interaction causes an increase in velocity between the aerofoil and the ground as the aerofoil height decreases. This in turn causes a drop in pressure and so causing an increase in downforce. At extremely low heights the aerofoil and ground boundary layers overlap and a stall condition results. This is discussed by Zerihan and Ranzenbach and Barlow [4, 5]. These conclusions were made from the experimental data obtained which were taken from a wing with large end plates. This area of stall is also demonstrated by Zerihan where the C_L data shows a dramatic decrease in the amount of lift being produced when the wing is brought into the region where the diffuser section becomes severe. Possible contributing three-dimensional effects are discussed further on.

Results presented by Dominy [16] show the effect on the pressure distribution over the front wing when operating in ground effect. A large increase in the C_P value occurs in ground effect compared to the same wing in freestream, as seen in fig.2.

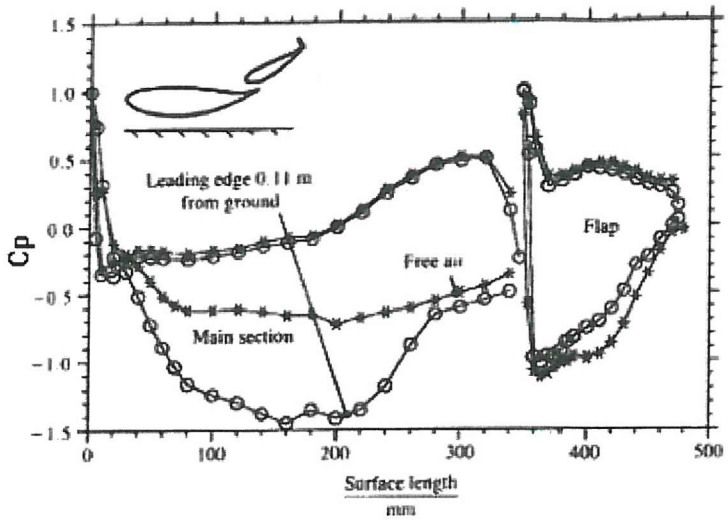

Figure 2. The effect of ground proximity on the pressure distribution over a front wing, Dominy [16].

Jasinski and Selig [7] carried out two-dimensional and three-dimensional experiments on a two-element configuration over a range of Reynolds numbers and incidence angles. Reynolds numbers effects were found to have very little impact on the results. The lift and drag varied only about 3-4% over the range of Reynolds numbers tested (a factor of 2 variation). Pressure readings were not compared for different Reynolds numbers, but for a single Reynolds number it was shown that the C_P plots do show variations for different angles of attack.

Ranzenbach and Barlow [4, 5] completed simulations on a two-dimensional wing in ground effect using a Reynolds-Averaged Navier Stokes (RANS) solver for a single element NACA 0015 and NACA 4412 wings. They showed that the computations compared well with their

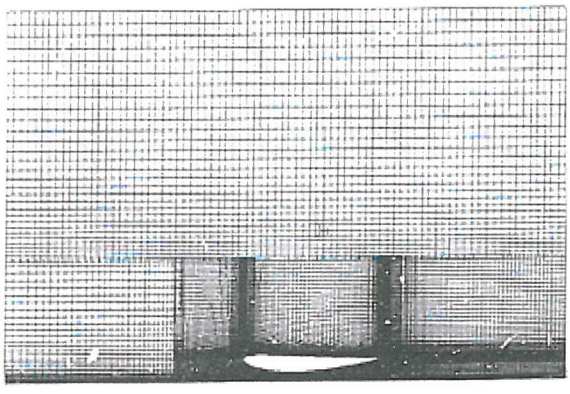

Figure 3. Grid used by Ranzenbach and Barlow on an inverted NACA 4412 in ground effect [10].

experimental measurements of downforce produced with a fixed ground. They used an entirely structured grid as shown in fig.3. This grid produces large variations in grid densities throughout the region. It can be seen that a C-type grid was not used due to the

lack of stretching in the grid region just upstream and above the leading edge. This is an area where stretching would occur if a C-type grid is implemented.

As discussed by Zerihan for a single element wing in ground effect, the image effect and the diffuser effect are both important. In the image approach, the image aerofoil is placed beneath the ground plane at a height equal to that of the real aerofoil from the ground. This makes the ground a symmetry line between the real aerofoil and the image. The circulation of the image aerofoil is in opposition to that of the real aerofoil. Therefore, the circulation of the image aerofoil will induce a positive stream-wise velocity over the actual aerofoil, and thus reduce the pressure, particularly on the suction surface compared to the freestream case. However, the strength of this induced effect is greatly dependant on the distance from the ground. A drawback to this theory is that it only considers inviscid effects and is two-dimensional. When applied to the real viscous physics, it implies that the ground would have a greater velocity than that of the freestream and so the moving ground effects become distorted.

The diffuser approach is where only the real aerofoil is considered for downforce-producing wings in ground effect. This approach considers that the flow will accelerate around the lowest point on the suction surface to the ground (contraction section) and diffuses through the gradual expansion section. The flow velocity increases leading up to the region of the contraction/expansion change-over and so downforce is produced. Following this is a region of separation. This not only explains the surface pressure distributions, but also the movement of the suction peak forwards from the position observed in freestream due to the increased velocities experienced closer to the ground.

1.4.6 Three-Dimensionality

Zerihan found that as the height is reduced the three-dimensionality of the flow increases. The higher levels of suction feed a stronger tip vortex. In contrast to this conclusion, at a height below h/c = 0.134, results found by Zerihan show a sudden reduction in the vortex strength. The closeness of the ground limits the roll up of the vortex. Jasinski and Selig [7] stated that the presence of an end-plate increased downforce, with an even greater performance increase experienced by using a larger end-plate. They found that a lack of end-plate area allowed the trailing vortex to roll-up earlier and so produced more induced drag and less downforce. The surface pressures also indicated this effect of flow three-

dimensionality decreasing. However, the reduction in tip vortex strength was not seen to have an adverse effect on the overall level of downforce.

1.5 Reynolds-Averaged Navier Stokes Models

The Reynolds-Averaged Navier Stokes (RANS) turbulence models used for this project include the Launder-Sharma k-ε model [20, 21, 22], the k-ω (Wilcox) model [20, 23], the hybrid k-ω/k-ε Shear Stress Transport (in future k-ωSST) Menter model [24, 25, 26, 27], and the Spalart-Allmaras (SA) model [17, 18, 19, 36]. The reason for choosing these models was their widespread industrial use and availability. In the case of the SA model, it allows for the future development and comparison of a Detached Eddy Simulation (DES) model and results, as described by Nikitin et al [35] for an aerofoil at a high angle of attack [18, 39, 43].

1.5.1 The k-ε Two-Equation Turbulence Model

The two-equation k-ε model originated in the 1972 publication of Jones & Launder [21]. The most widely used version of the k-ε model is that presented by Launder & Sharma in their 1974 [22] paper.

However, a problem with the k-ε model is the performance when dealing with a non-slip boundary condition. The k-ε model inherently over-predicts the near wall value of the eddy viscosity. As this is critical in the calculation of skin friction and the prediction of separation, near wall modifications are required. The early fixes were in the form of wall functions, but these fairly rough corrections assume the turbulence and the mean velocity follow set profiles. These are then modelled by the k-ε model away from the wall. The solution of complex flows is problematic for these wall functions as the profiles do not follow those prescribed.

1.5.2 The k-ω Two-Equation Turbulence Model

The k-ω model was presented by Wilcox [23] in 1988. This is a two-equation model using k and ω as its typical scales. This model has been shown to produce favourable results near

solid boundaries. However, it has been shown by Menter [25], that the k-ω model is sensitive in the free stream region. Further studies by Bardina et al. [28] further demonstrate these conclusions, showing large dependency on free stream turbulence values.

1.5.3 The k-ωSST Two-Equation Turbulence Model

The k-ωSST model was first implemented by Menter [24] in 1994. This model combined the k-ε and k-ω models into a single model. By combining these models, the near-wall advantages of the k-ω model could be utilised while running the k- ε model in the free-stream region. To this end, Menter transformed the Launder-Sharma k-ε model into a k-ω form and then blended it with Wilcox's 1988 version of k-ω.

The k-ωSST model has been subjected to rigorous testing both in Menter's own paper [24], Bardina et al. [28], Klausmeyer & Lin [19], Kim et al. [44] and Godin & Zingg [45]. In these studies the SST model is shown to outperform most models tested especially in cases of large separation or complex geometries.

1.5.4 Spalart-Allmaras One-Equation Turbulence Model

The Spalart-Allmaras model (SA) was developed by P.R. Spalart and S.R. Allmaras [17]. The philosophy behind the development of this model was that the process of simplifying a k-ε model is not the best approach. However, a one-equation model that is designed from basics and calibrated empirically would prove to be more useful. In building up the model by using increasingly complex flows, the result is a model which has been shown to perform well as described by Bardina et al.[28] where it out-performed many two-equation models.

1.5.5 Computational Comparative Studies

In a study by Bardina et al [28], the grid sensitivity and the sensitivity to the initial and boundary conditions using various models was investigated. Of the flows tested, seven had relatively simple free-shear and zero-pressure-gradient boundary layers and three were

relatively complex flows involving separation. They compared the k-ε model, the k-ω, the k-ωSST and the SA models. The models were ranked by Bardina et al [28], in terms of relative performance. The k-ωSST model is perceived to produce the most accurate results, followed by the SA model, the k-ε model and finally the k-ω model. However, these rankings are based on overall performance on numerous flow types consisting of simple free-shear and zero-pressure-gradient boundary layer flows and some relatively complex flows involving separation. In the complex flows it was found that the k-ε model performed worst of all followed by the k-ω model. These conclusions by Bardina et al [28] will be confirmed in this study as the performance of each of these models will be ranked based on a wing in ground effect flow.

Several other studies have confirmed this pattern and more specifically with regard to high-lift airfoils. These studies include single, double and triple element up-lifting airfoil configurations. Kim et al [44] utilised the k-ε, k-ω and the k-ωSST models. The test geometries included a NACA 4412, a NLR 7301 and the NASA GA(W)-1. Results indicated that the k-ωSST model showed better performance compared to the other two-equation models in predicting the adverse pressure gradient region over the suction surface of the high-lift airfoils. A similar study by Godin & Zingg [45] using the S-A and k-ωSST models on an undefined single element airfoil at high angle of attack. Also included in the study were the NLR 7301 and the NASA GA(W)-1. Again, the k-ωSST model was found to provide the most accurate results in separated flow regions, whereas the S-A model was more accurate in attached flows and wakes. A conclusion is made by the authors that the S-A model is preferential when studying take-off wing configurations while the k-ωSST model should be preferred in landing configurations. Another study detailed in the report by Klausmeyer & Lin [19] shows that RANS models perform relatively well compared to experimental results over high-lift airfoils.

1.6 Detached Eddy Simulations

1.6.1 Detached Eddy Simulation Overview

DES is a three-dimensional unsteady numerical solution using a single turbulence model (unlike Unsteady RANS, DES cannot be performed on a two-dimensional grid). This model functions as a Sub-Grid-Scale (SGS) model in regions where the grid density is fine enough for Large Eddy Simulations (LES) [32]. It also operates as a RANS model in

regions where the grid density is not fine enough. SGS or LES is used wherever the grid density allows, with the self-adjusting model invoking a lower level of mixing, relative to the RANS model, in order to explicitly resolve the larger-scale instabilities in the flow. In other regions, mostly the boundary layers, the RANS model is used. There is only a single velocity and model field in use and as such there is no issue of smoothness between regions [38].

DES is aimed at the prediction of separated flows for a wide range of Reynolds numbers and a reasonable cost in engineering applications, by combining a fine tuned RANS model in the boundary layer with LES in the separated regions. Since the large eddies are resolved, increased grid refinement expands the range of scales in the solution, and thus the accuracy of the non-linear interactions captured by the solution. The cost of DES is so far demonstrating itself to be feasible. Shur et al [18] used a personal computer for DES of an airfoil at high angles of attack and quite high Reynolds numbers.

It is therefore also likely to be useful for simulating wing in ground effect flows with which we are interested. One motivation for this study is to determine the extent to which DES can be used as a practical and efficient design tool for, for example, the motorsport industry. However, to make good use of DES in geometries such as a wing in ground effect, it is essential to first have an understanding of the physics as well as knowledge of the performance levels of two-dimensional steady and unsteady RANS turbulence models with which DES is competing. This motivates the objectives listed above, which will provide performance benchmarks and allow clear demonstrations of any gains achieved using DES.

Chapter 2
Approach

2.1 Research Strategy

A central task in any Computational Fluid Dynamics (CFD) study is to build a quality grid and analyse its effect on the accuracy of the solution. This can be a very tedious and time consuming process. Tests must be carried out on the same grids for a range of RANS turbulence models and for a variety of heights from the ground. Results are then compared to an appropriate benchmark which for this work we take to be the experiments of Zerihan. Although the optimal grid design can vary depending upon the RANS model used, our grids were designed primarily with the SA model in mind. This is due to the plan to eventually implement a DES code using the SA model. Because a quasi two-dimensional region of flow exists near to the centre of the wing [9], the centre line results are used to compare with our two-dimensional CFD results. We focus upon the surface pressure distributions and net lift and drag coefficients.

When this study began, our plan was to use CFL3D as our primary computational tool. Results from this phase of the project are presented in Chapter 3. Since we eventually decided to complete the work using Fluent (for reasons given below) the bulk of this chapter will be presented in terms of Fluent variables and procedures.

2.2 Single Element Wing/Aerofoil

The single element wing/aerofoil used in this project has the same profile as that used by Zerihan, namely the main element of the 1998 Tyrell 026 F1 car front wing. Due to wind tunnel restrictions, Zerihan used an 80% model of the Tyrell 026 front wing. This gives a wing chord c of 223.4mm, which is constant across the wing, and a wing span of 1100mm, thus maintaining the original aspect ratio. The wing has a finite trailing edge, of thickness

1.65mm (0.007c). Zerihan also used generic endplates which were chosen to allow testing at very low ground heights. The wing co-ordinates are given in Table 2 (Appendix).

The wing was originally developed from a NASA GA(W) profile, type LS(1)-0416 MOD, as shown in fig.4. Through communication with the Tyrell Racing Organisation, Zerihan discovered that the camber of the suction surface was reduced, and the lowest point on the suction surface was moved forward. The pressure surface was flattened, thus increasing the pressure on it. A modification was also made to the leading edge [9].

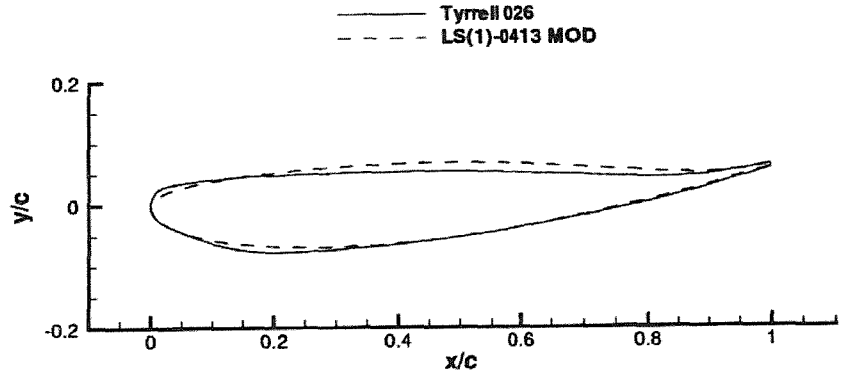

Figure 4. Aerofoil profiles: Tyrell 026 aerofoil and NASA GA(W)-2 LS(1)-0413 MOD profiles [9].

2.3 Wing Height and Incidence

We consider conditions first used by Zerihan. The ride height is defined as the distance from the ground to the lowest point on the wing, with the wing incidence set to zero degrees. The height the wing varies is between 0.672 to 0.089 h/c. Having set the height, the wing is rotated about the quarter chord position. The majority of the Zerihan tests were at an angle of incidence of 1degree, nose down, using rotation about the quarter chord position. This corresponds to the endplates being parallel to the ground.

2.4 Flow Solvers

The packages used are summarised here for future reference.

2.4.1 Computational Fluids Laboratory 3-Dimensional (CFL3D) (Version 5.0)

This code was developed by Krist, Biedron and Rumsey at The Aerodynamic and Acoustic Methods Branch of The NASA Langley Research Center, Hampton, VA, USA. The code solves the time-dependent, compressible, conservation form of the Reynolds-Averaged thin-layer Navier Stokes equations on structured grids. The spatial discretisation involves a semi-discrete finite-volume approach for variable, $q= (\rho,u,v,w,p)$ at cell centres. Upwind-biasing is used for the convective and pressure terms with either the flux-vector-splitting of Van Leer or the flux-difference-splitting of Roe. Central differencing is used for the shear stress and heat transfer terms. Time advancement is implicit with the ability to solve steady or unsteady flows. Multigrid and mesh sequencing are available for convergence acceleration. Numerous turbulence models are provided, including inviscid, laminar and the Baldwin-Lomax, SA, k-ω and the k-ε turbulence models. Multiple-block topologies are possible with the use of 1-1 blocking, patching, overlapping, and embedding. Boundary conditions can be set over subsets of block faces. CFL3D does not contain any grid generation software. For further details see [41].

2.4.2 Fluent (Version 6.0)

Within Fluent, both structured and unstructured grids are available. All speed regimes (low subsonic, transonic, supersonic, and hypersonic flows) are incorporated into the package. An inbuilt parallel processing facility exists and both steady-state and unsteady-state solutions can be run. Fluent can cope with various flow properties and has a large materials properties database. Numerous turbulence models are available, including simple k-epsilon, SA and k-ω models. A dynamic mesh capability is provided for modelling flow around moving bodies.
Fluent includes a Grid Generator (Gambit) and also a comprehensive post-processing interface. Further details are given in [42].

2.5 Turbulence Models

Both CFL3D (Version 5.0) and Fluent (Version 6.0) contain a range of turbulence model options, allowing comparison between CFD and experimental work for the various models. The turbulence models included in this study are the SA one-equation model [17, 18, 19], the k-ε model [20, 21, 22], the k-ω model and the k-ωSST model [20, 23, 24, 25, 26, 27]. As mentioned earlier, the study by Bardina et al [28] demonstrated that the k-ωSST model performed best for a collection of basic aerodynamic flows. The SA model was found to perform the best based on grid spacing required for accurate solutions. The k-ωSST model was found to have the greatest overall performance for the more complex flows. We expect therefore that it will also perform well here. The ability of each of these models to capture the wing in ground effect flow will be quantified below.

2.6 Boundary Conditions

The boundary conditions used in each simulation are presented in fig.5. The upstream boundary is modeled using the Velocity Inlet condition specified in Fluent. This allows the freestream velocity to be specified. The downstream boundary is modeled using the Pressure Outlet condition. This is used to ensure that no back flow can occur by ensuring the pressure difference across the boundary remains equal to zero. The upper domain boundary is set as Symmetry, setting the velocity across this boundary to zero. The aerofoil surface is specified as a No-Slip Wall. The ground is specified as a Moving Ground with a velocity equal to that in the freestream of 30m/s. In certain simulations, such as the stationary ground runs, the ground was specified as a No-Slip Wall.

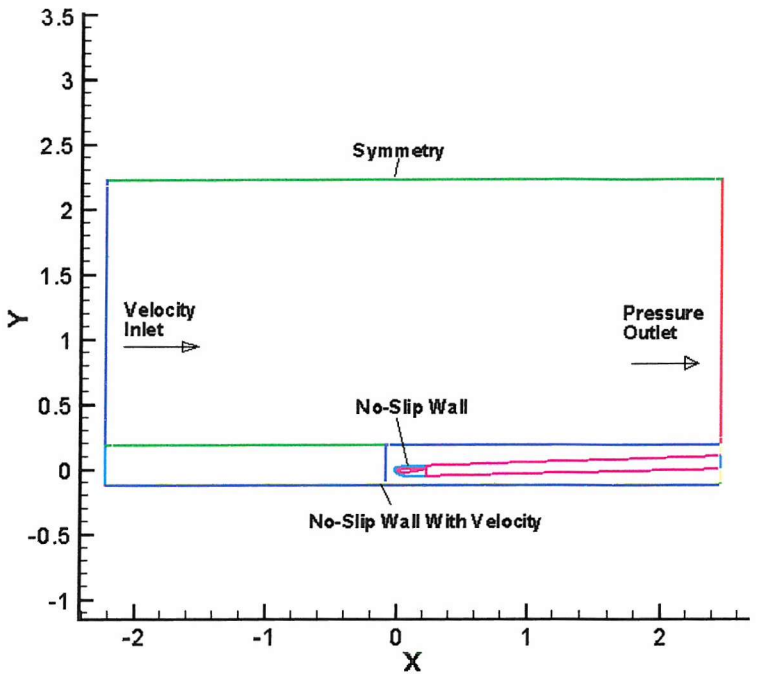

Figure 5. Fluent Grid Layout detailing Boundary Conditions set.

2.7 Reynolds Number

Based on the limitations placed upon Zerihan, the speed of the rolling road in the wind tunnel had to be kept at 30m/s for all tests. Through measurements, showing a constant dynamic pressure of 56.25mm water, corresponding to $U_\infty \approx 30$m/s, the Reynolds number based on the wing chord falls in the range of $0.430 - 0.462 \times 10^6$.

In relation to current racing car testing where models in the region of 50% scale are typically used at speeds up to 40m/s, the model used by Zerihan was an 80% scale model. This gives a Reynolds number in the range of approximately 20% to 50% higher than current racing car model testing.

2.8 Computational Strategy

In order to both validate the solutions and to provide useful insight into this problem, we developed a baseline grid that yields reasonably accurate results. We then adapted this grid by adding and removing points and assessing the grid dependence of the problem. We consider four different models at seven ride heights using three grid densities for two-

dimensional simulations. This study provides a database illustrating the effects of numerical and physical parameters on wing in ground effect flows.

2.9 Analysis Methods

The grid validation is carried out by comparing results with the experimental data of Zerihan. We examine the Coefficient of Pressure (C_P) distribution for each model at all grid densities coupled with ride heights between 0.672 to 0.089 h/c.
The dependence of the Coefficient of Lift (C_L) against h/c is also compared, which demonstrates how well each solution captures the downforce variation induced by the ground. We are particularly interested in the characteristic plateau and sudden drop in downforce observed by Zerihan as h/c tends to zero.
Another method for comparison is the Coefficient of Drag (C_D) against h/c. High downforce implies fast cornering and stability but the trade off is high drag, which will slow the straight-line speed. The optimum balance will vary greatly from circuit to circuit and therefore a continuous assessment of these factors is critical.

The preliminary computational results of Zerihan will also be utilised in order to highlight the effect grids and computational packages can have on the solution.
Further analysis of the results will be presented below in order to gain an insight into the physics of wing in ground effect flows.

Chapter 3
Grid Generation

3.1 Grid Development

This chapter deals with the development, modification and problem solving involved in producing a grid to work with either CFL3D or Fluent. As both computational packages can utilise a grid developed through third-party software, it was decided that in order to isolate the effect of the solvers, the same grid would be used for both. This was created by Gridgen [29]. The software can generate both structured and unstructured grids. The aerofoil geometry is input by reading a file containing co-ordinates supplied by Zerihan (see Appendix, Table 2).

The grids are created by initially specifying a four-sided closed domain or flow area which surrounds the test geometry. This is then given grid points by allocating a number of points to each side. For a structured grid, opposing faces must have equal numbers of points as they map directly onto each other. However, unstructured grids do not require this and therefore provide greater flexibility when trying to minimise the overall number of points. This is achieved by having large numbers of points close to the ground. On the opposite side, namely the upper edge of the domain, the number of points can be greatly reduced. As this region is in the freestream the effect of having very few points is not detrimental. Structured grids therefore are penalised by being forced into a larger than necessary grid-point count. These points can be distributed, but normally there is always a degree of waste concerning excessive grid point densities.

With a combination of both structured and unstructured grids the flexibility to adapt to complex geometry is improved. By using a structured grid on any boundary layers, a greater accuracy in the solution is achieved. This is then supplemented by the adaptability of the unstructured grid in areas where stretching might occur if using structured grids. The number of grid points is also reduced by having this combination. This allows very fine

grid sections along the boundary layers while reducing the grid points elsewhere in the domain.

3.2 CFL3D Grid Development

Various combinations of grid types and composition were used in achieving the results for validation of both the grids and the flow solver. Structured grid types such as H-type, which are rectangular shaped, C-Type, which wrap the grid points around the aerofoil in a subdomain shaped like the letter "c" and O-Type, which completely surround the aerofoil with an o-shaped subdomain, were all used in different combinations in order to achieve the best possible grid layout and results. The C-type grid is specifically used for curved surfaces and thus is particularly suited to an aerofoil. However, this can cause problems with grid stretching when a flat surface (in this case the moving ground) is close to the curved surface of the wing. When using structured grids alone, this stretching can become a major problem. To remain accurate, the grid needs to ideally have 90° angles at the corners of each grid cell with no more than a 120° stretching allowable. This figure of 120° is only a guide as even this can cause problems inaccuracies. Flowfield features such as reduced velocity, also manifested as increased pressures, occur in areas where grid stretching is extreme. These anomalies appear in areas where no such features are expected, such as in the freestream areas upstream of the aerofoil. Rigorous grid refinement and the addition of more grid points can be used to mitigate this problem but it is never completely removed, merely minimised. This caused great problems in the CFL3D grids where the aerofoil is close to the ground. The areas which experienced the worst stretching were the corners of the C-type grid where they are required to be square rather than rounded (as they would normally be) due to the flat ground. In order to overcome this problem large numbers of points were clustered in these regions. This then also adds to the computational cost.

The first grids to be completed were those for the freespace simulations for the NACA 0012 and NACA 4412. The topologies of the first set of grids to be tested were crude in that they comprised basic distribution and layout. As seen in fig.6, both C-type grids and H-type grids were used in varying combinations. These grids use the Tyrell-26 aerofoil but virtually exact copies were used on the NACA geometries.

Figure 6 (a) comes from grids used by Zerihan and shows the stretching which occurs when using a square sided C-type grid. The points on the boundary layer are mapped onto the leading edge of the grid. This stretching can be decreased by mapping some of the points onto the top and bottom edges of the grid but this introduces stretching at the corners of the

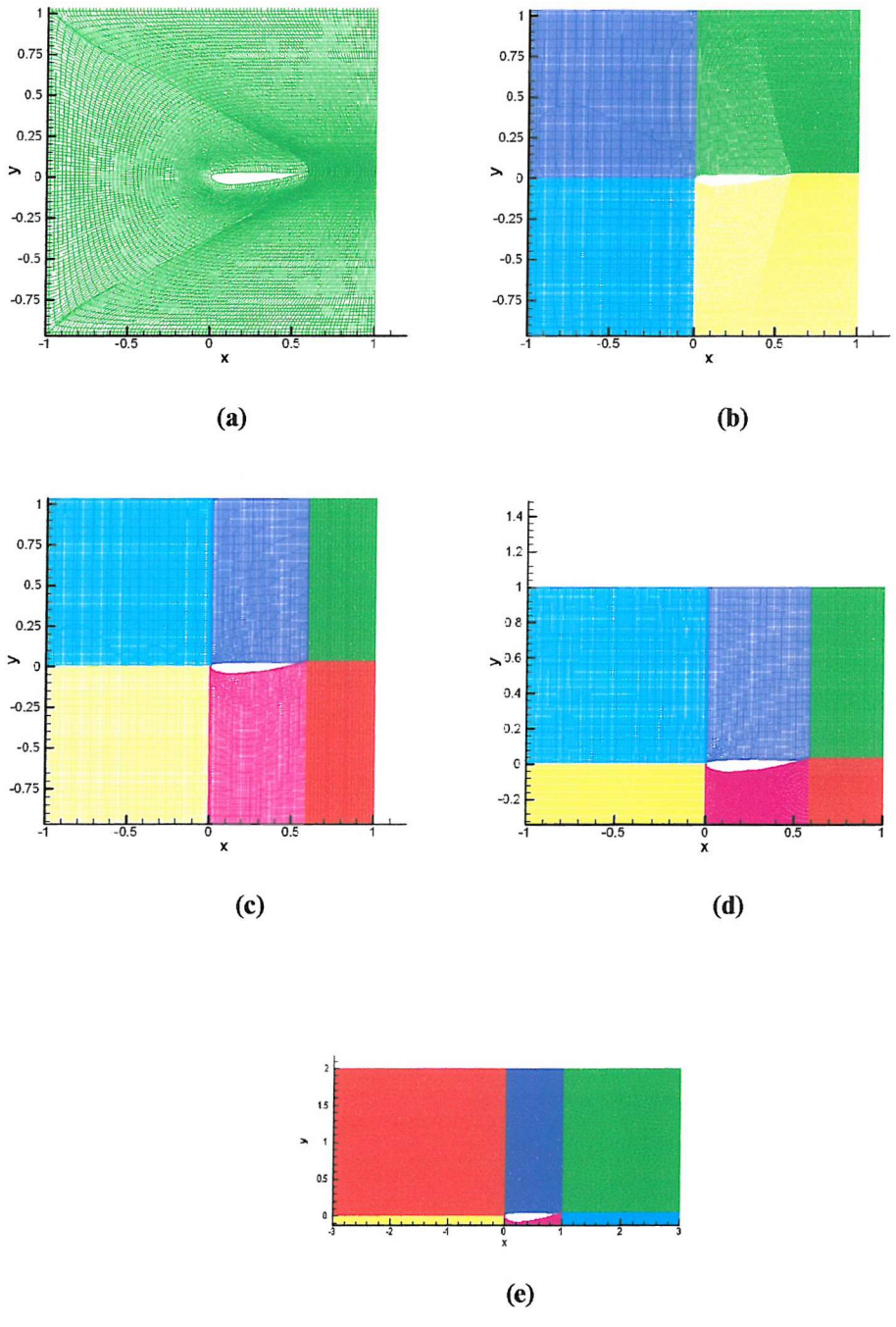

Figure 6. CFL3D Grids (a) Consisting of a square C-Type grid with a rectangular trailing-edge grid. (b), (c) and (d) comprise various numbers of rectangular grids, attempting to avoid the problems caused by the curvature of the airfoil affecting the grid lines. (e) Shows a similar configuration of the grid in close proximity to the ground (All grids surround Tyrell-26 wing).

leading edge. Figure 6 (b) to (e) show the grid developed from those of Ranzenbach and Barlow [10], shown in fig.3. The final grid for the wing in freespace, whether it is the Tyrell-26, the NACA 0012 or the NACA 4412, used the layout presented in fig.7. This comprised a C-type grid around the wing with an H-type grid included to accommodate a blunt trailing edge when it is present. The darker sections indicate how the grid is clustered near the leading edge and the trailing edge. Figure 8 shows a close-up view of this grid when applied to the NACA 4412 geometry.

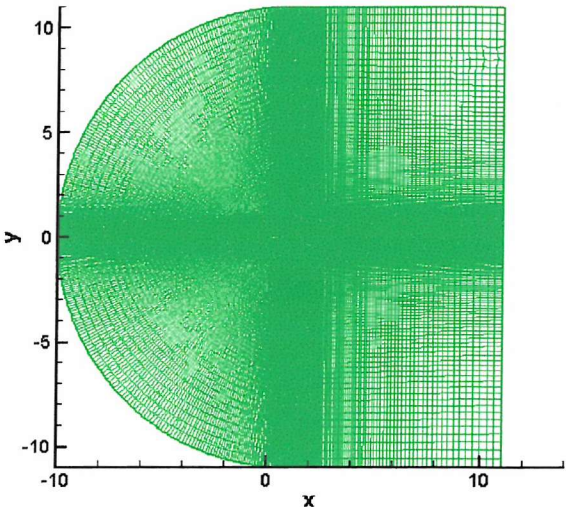

(a)

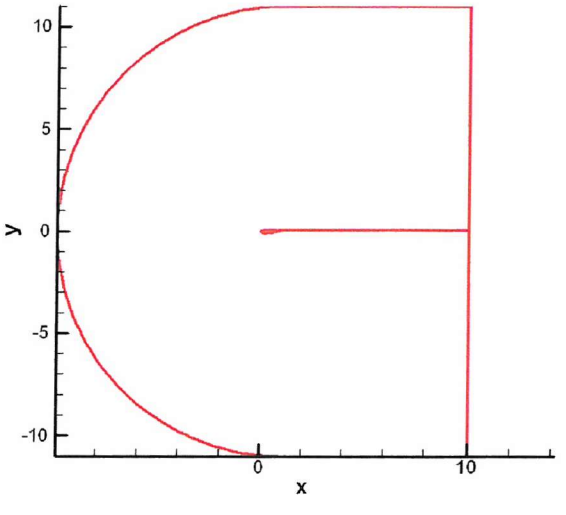

(b)

Figure 7. CFL3D Grid, (a) The final two-dimensional grid, comprising a circular C-type grid with a rectangular trailing-edge grid. (b) The same grid with only the grid boundaries shown (Grid surrounds Tyrell-26 wing).

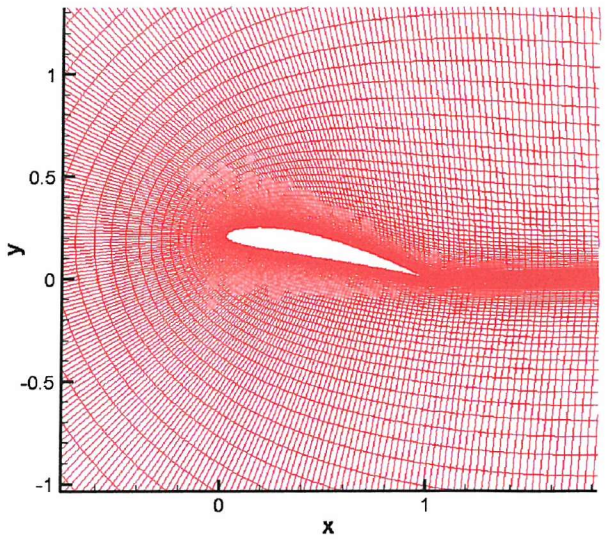

Figure 8. CFL3D Grid: Close-up view of the NACA-4412 grid showing the 12° angle of attack of the aerofoil.

When the wing-in-ground-effect cases were first attempted, it was found that few of the lessons learnt from the freespace grids could be directly applied to the ground-effect grids. The main reason for this is the height from the ground being in the region of 0.7 to 0.1h/c of the lower rounded surface of the wing. The grid has to be adapted to incorporate both of the curved wing surface and the flat ground, over a very small distance. This prevented the C-type grid from utilising the most efficient curved grid lines near the ground. This then caused severe stretching in the corners of the C-grid subdomain. It was counteracted by severe redistribution and the addition of extra points over a large number of grid iterations. The final grid layout is shown in fig.9. It can be seen that the region surrounding the aerofoil has very high grid point densities compared to the regions outside this critical area. In fig.9, Blocks 4 and 5 are very narrow grid sections. Block 4 covers the ground boundary layer and Block 5 covers the region from the blunt trailing edge of the aerofoil. The location of the ground in each image can be found at approximately y = -0.6.

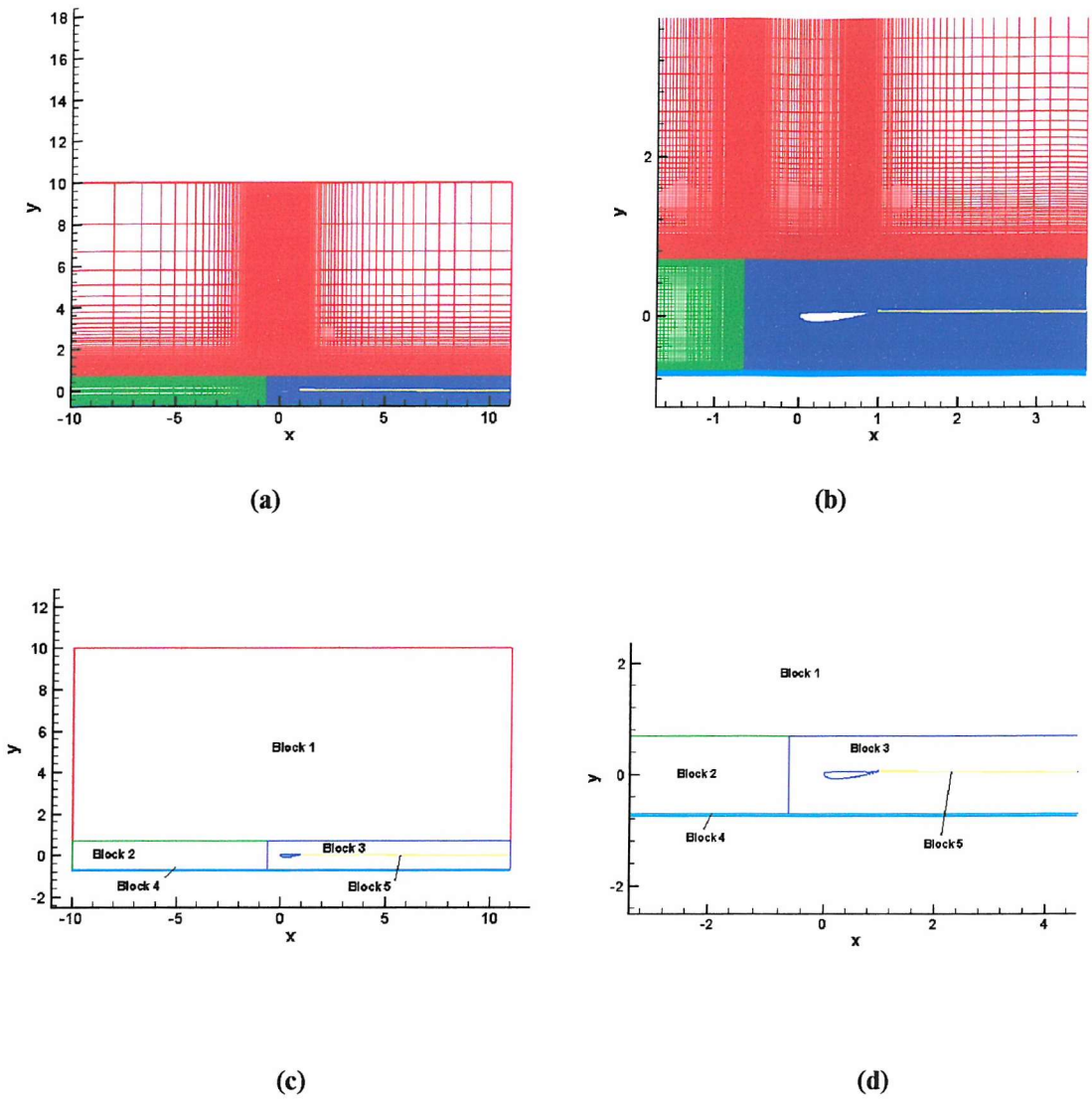

Figure 9. CFL3D Results: (a) Complete view of grid used for a height of 150mm. (b) Zoomed in view of grid used for a height of 150mm demonstrating the Square C-Type grid. (c) Block layout and numbered. (d) Close-up of the airfoil showing block numbering scheme.

Figure 10 shows the grids developed for the Tyrell-26 aerofoil in ground effect for use with CFL3D. In fig.10 (a) to (d) the development process and changes to the problem areas of the moving ground grids are illustrated.

It is seen that for the coarser earlier grid, the grid-lines close to the corners curve and hence the angles of the grid-line intersections exceed 120°. In the finer redistributed grid, this grid-line curvature is removed and the grid stretching is minimised though not removed entirely. A problem associated with adding grid points to overcome the problem of grid

stretching is the possible excessive clustering of points in certain areas causing a loss in efficiency. This can be seen forward of the leading edge (fig.10 (a) and (b)) as diagonal lines of clustered points.

While also present in the coarser grid, the excessive clustering is more of a problem in the fine grid where the grid needs to have gradual changes in grid cell size otherwise it is likely that flow anomalies will occur. The final grid iteration had approximately 275,000 points. This is quite a large number especially when compared to that of the grids used later in the Fluent calculations. This is one of the costs of using structured grids alone. An additional cost is the time taken to produce a grid with little or no stretching effects. This cost can be very substantial.

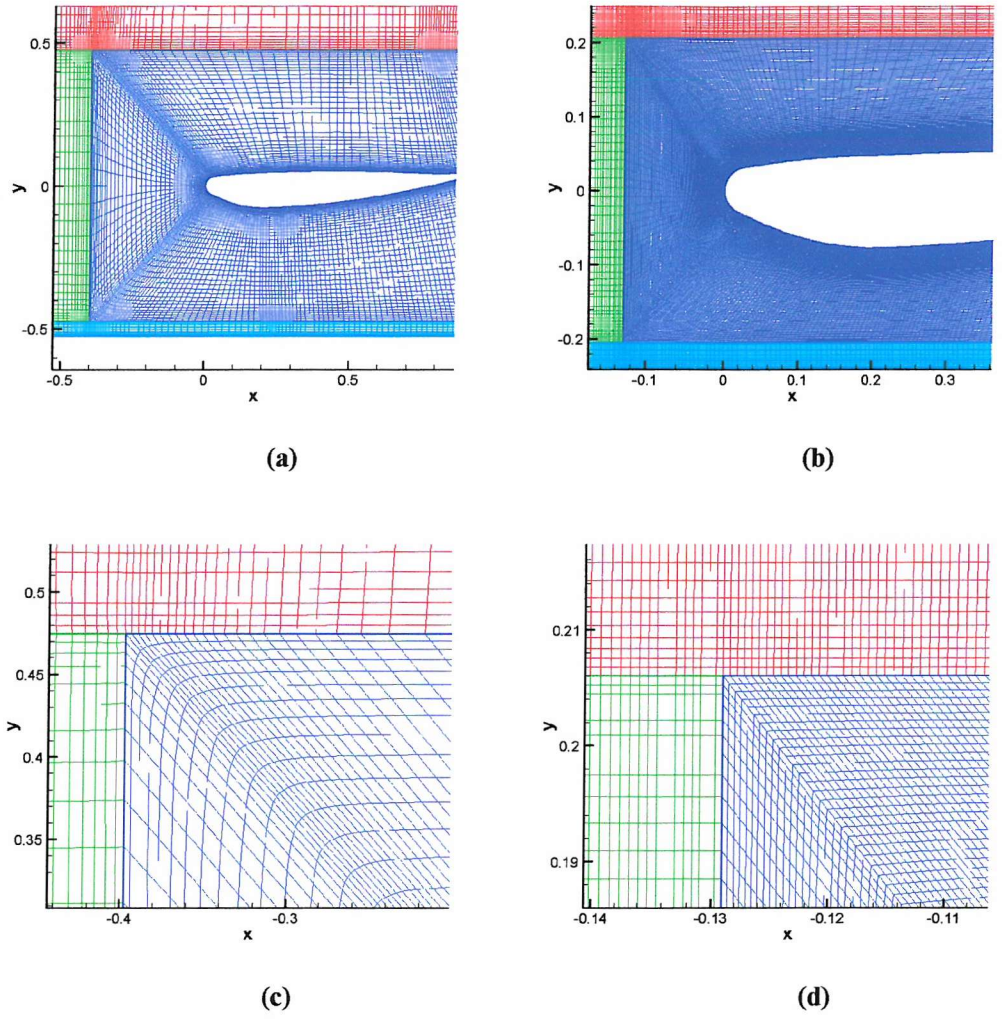

Figure 10. CFL3D Grids (a) Coarse grid demonstration areas of severe grid stretching, 50mm ride height; (b) Fine grid demonstrating areas of grid stretching, 40mm ride height; (c) Coarse grid showing grid stretching, 50mm ride height; (d) Fine grid demonstrating corrected grid stretching, 40mm ride height.

3.3 Fluent Grid Development

When using a combination of structured and unstructured grid types, the problem of grid stretching can be overcome. This is done by using a fine structured grid close to the curved wall, and before any major stretching can occur changing the grid to an unstructured type. As explained earlier, grid refinement is a long and laborious process requiring subtle changes to the layout and distribution of the grid in order to achieve maximum accuracy. A range of grids is also needed to demonstrate the robustness of the Fluent solver. Grids using various layouts and numbers of points were therefore considered.
The strategy best suited to wing-in-ground-effect flows is presented in fig.11 (a) to (c), where plots show the layouts and distributions developed in order to achieve the best possible results from the various aerofoils. The grid contains six blocks in total with two being structured grids and four unstructured. The unstructured grids were used in areas where fewer points were needed (the upper region of the computational domain) and where large amounts of stretching was expected (for example in the region between the curved lower-aerofoil surface and the ground). Clustering of points near block boundaries was utilised due to experience gained with the CFL3D grids. If clustering wasn't incorporated, anomalies appeared at these boundaries. A C-type structured grid was utilised around the aerofoil in order to achieve the greatest control over the number and distribution of the points. This allowed location of an optimum number of grid points near the aerofoil surface.

Points are clustered towards the leading and trailing edges, coinciding with the distribution of the points in the adjoining unstructured domains. The C-type grid was based on the aerofoil shape, by scaling up the aerofoil co-ordinates and mapping the points from the aerofoil onto a larger section of itself, thus keeping as structured a grid as possible. The grid section that runs the length of the ground is also of a structured type, in order to utilise the fine grid necessary in this region to resolve any boundary-layer features present.
This grid layout is applied for each ride height with slight modifications for grids of $h/c = 0.134$ and below, which include raising the ground towards the aerofoil and slight narrowing of the C-type grid to accommodate the smaller region between the suction side and the ground. The grid points were also redistributed to allow for similar grid density in the regions where the spaces between the grid blocks became limited, as illustrated by fig.11 (c) and (d).

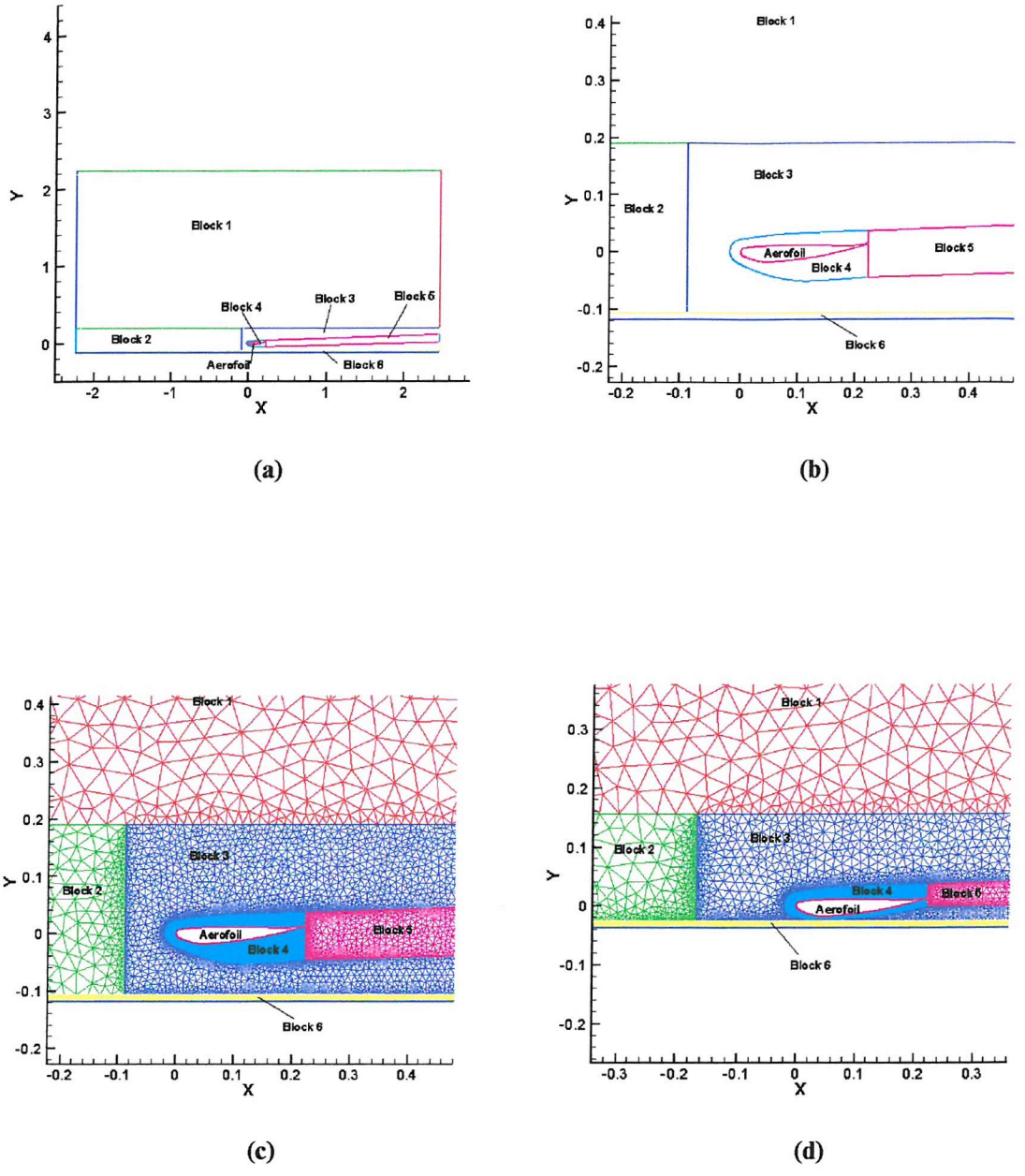

Figure 11. Fluent Grids (a) Full Grid with Labelled Blocks/Grid Zones for 100mm Ride Height Case, ground at y = -0.12; (b) Close-up of layout detailing Aerofoil for 100mm Ride Height Case, ground at y = -0.12; (c) Close-up of layout detailing Aerofoil including Mesh/Grid Points for 100mm Ride Height Case, ground at y = -0.12; (d) Close-up of layout detailing Aerofoil including Mesh/Grid Points for 20mm Ride Height Case, ground at y = -0.04.

3.3.1 Grid Densities

The grid densities are listed in Table 1; the main differences involve the C-Type structured grid section around the aerofoil. This is because it is this section that has the greatest impact on solution accuracy and run times. This was examined by running several simulations with various grid densities and investigating the distribution of C_P and C_D. As a consequence, the grid density in this region is substantially higher than other individual regions and directly affects the run times of the solution. Another crucial region is the wake. The wake density is changed automatically by changing the density of the C-type grid section mentioned above, as can be seen in fig.13.

	Grid Points	Aerofoil Structured Section
Coarse	~ 65,000	201x 41
Standard	~ 95,000	401 x 81
Fine	~ 135,000	601 x 121

Table 1. Grid Densities for Two-Dimensional Grids

Chapter 4

Two-Dimensional Steady-State Simulations

4.1 Introduction

In this chapter the two-dimensional results obtained using both the CFL3D and Fluent packages and using the k-ε, k-ω, k-ωSST and the SA models are presented.

The Fluent simulations include four turbulence models with various ride heights and grid densities for the aerofoil detailed above. The CFL3D work varies from this slightly and is dealt with separately in the next section. All cases are fully turbulent

4.2 CFL3D Results

The initial tests on the wing in ground effect flow were carried out using Version 5.0 of the CFL3D package. The reason for choosing this package was that the source code was available and could be modified to meet the requirements of this project. The initial plan was to modify the code to run DES and thus access to the source code was essential. CFL3D v.5.0 requires fully structured grids, which led to immediate difficulties even on the initial tests of wings in freestream due to the grid stretching problems described earlier. This issue becomes even more extreme for the wing in ground effect geometry. Simulations were run for the NACA 0012 and NACA 4412 aerofoils and compared to results of Amick [30] and Jansen [31, 32] respectively. After much grid development these solutions agreed quite well with those in the literature.

Results for the grid type in fig.7 are presented below and compared with the results of Amick [30] and similarly for the NACA 4412 results of Jansen [31, 32] for the grid type in fig.8. Figures 12 to 16 show plots of C_P versus x/c for the comparison with experimental results of Amick [30] on the NACA 0012, and the Large Eddy Simulations (LES) results presented by Jansen [31, 32] on the NACA 4412. The results are shown in order of increasing grid

refinement (clustering the points in areas which are seen as requiring better grid point resolution through trial and error development of the grids), such that the NACA 0012 results converge towards the Amick experimental results ($Re = 1.1 \times 10^6$). The same grid size (36,864 grid points) is used in both the NACA 4412 results where only grid refinement is different with $Re = 4.1619 \times 10^6$. The SA model was used in all these cases. The plots indicate reasonable accuracy for the leading edge region (note for example the expected symmetric C_P distribution on the top and bottom of the NACA 0012 at zero angle of attack, for a sufficiently fine grid). However, for the trailing edge the accuracy of the solution is poor. A concern is raised that with slight refinements in the grid layout, slightly more accurate results were produced but still not acceptable. This indicates a high level of grid dependency involving either specification of the airfoil surface geometry, distribution of the grid points or an inherent problem with CFL3D. However, at this point we note that it is possible to obtain a solution using CFL3D with these numerical and modelling parameters.

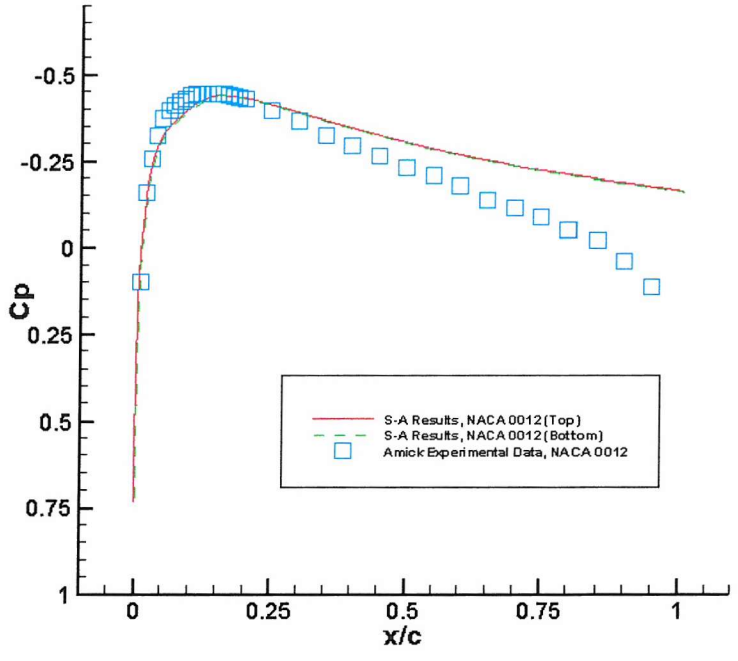

Figure 12. CFL3D Results: Plot of Coefficient of Pressure against x/c for the grid type in Figure 7 on the NACA-0012 airfoil at zero angle of attack with 23,040 grid points.

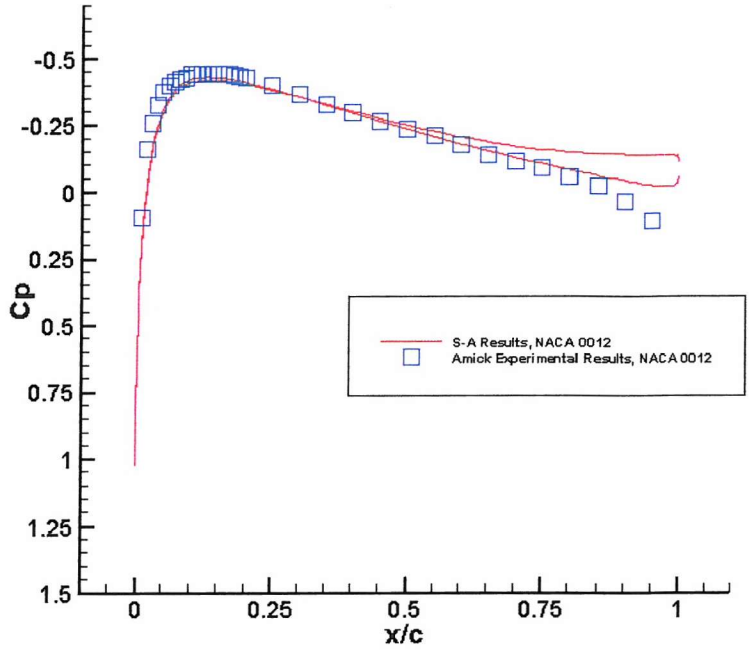

Figure 13. CFL3D Results: Plot of Coefficient of Pressure against x/c for the grid type in Figure 7 on the NACA-0012 airfoil at zero angle of attack with 36,864 grid points.

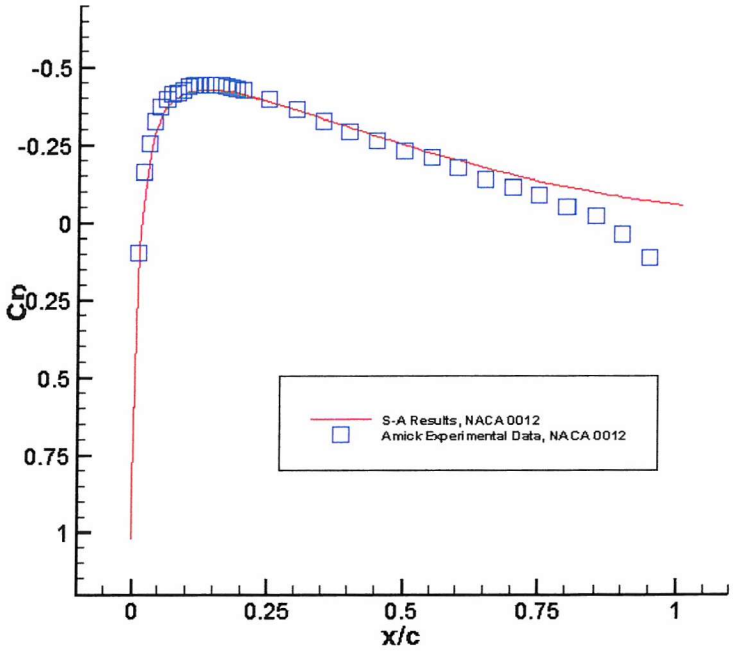

Figure 14. CFL3D Results: Plot of Coefficient of Pressure against x/c for the grid type in Figure 7 on the NACA-0012 airfoil at zero angle of attack with 36,864 grid points.

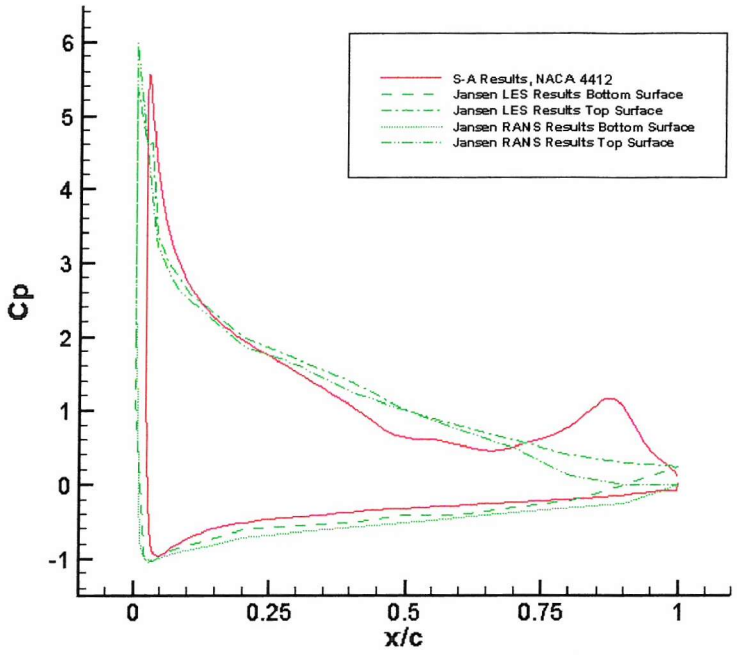

Figure 15. CFL3D Results: Coefficient of Pressure against x/c plot for the first simulation run with the NACA-4412 airfoil at 12° angle of attack with grid type as per Fig.8 and 36,864 grid points.

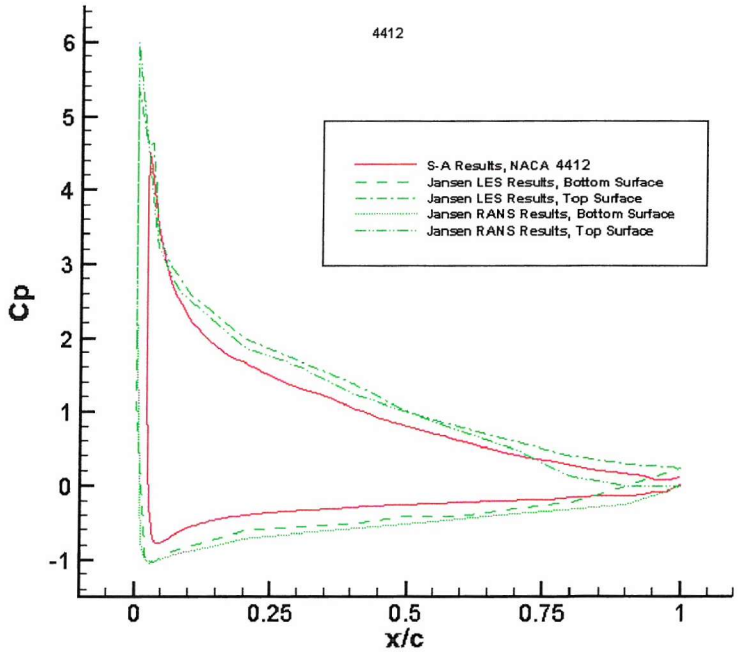

Figure 16. CFL3D Results: Plot of Coefficient of Pressure against x/c for a refined grid as shown in fig. 8 on the NACA-4412 airfoil at 12° angle of attack and 36,864 grid points.

For the wing in ground effect flows, the grids were developed as described earlier. With the grid problem minimised, steady state results were achieved which could be compared to the experimental results. However, because the package was designed for compressible flows and the present case is essentially incompressible, convergence was at times very difficult to achieve. Even when the solution appeared to converge, it was found that by running the solution further, the solutions would eventually begin to oscillate dramatically for all cases. The C_L and C_D values then showed signs of unsteady oscillations of a chaotic nature. This problem is also discussed by Milholen et al [33] and Zerihan. Milholen et al studied the differences between two compressible codes, one being CFL3D and an incompressible code. They found that for a free stream Mach number of 0.2, the incompressible code performed better in relation to computational cost for a simple wing section. However the compressible codes performed better on a fuselage and transport wing geometry. All the codes produced comparable pressure distributions and boundary layer profiles.

To alleviate this problem, Zerihan recommended the use of part steady-state part unsteady-state runs. This involved beginning in steady state mode until the initial perturbations in the solution were removed from the residual histories. The solution was then continued as an unsteady case whose end result was a solution which proved to be quite accurate in comparison to the experimental results. The optimal cut off point for the end of the steady and beginning of the unsteady runs was found empirically to occur after approximately 300 iterations, using the SA model. Typical C_P versus x/c plots showing a full steady state solution along with the combined steady/unsteady state runs are given in fig.17. Also shown is a plot of the residuals of the steady state solution allowed to run until 20,000 iterations to demonstrate the beginning of the divergence. The best of the steady state solutions were not as accurate as the combined steady/unsteady solutions. Therefore, the steady/unsteady methodology was found to be an acceptable way to overcome the problems with the compressible flow solver.

A plot of the respective C_L values against heights (fig.19) in comparison to data presented by Zerihan shows that good agreement can be obtained using this method. Plots for other heights are shown in fig.20.

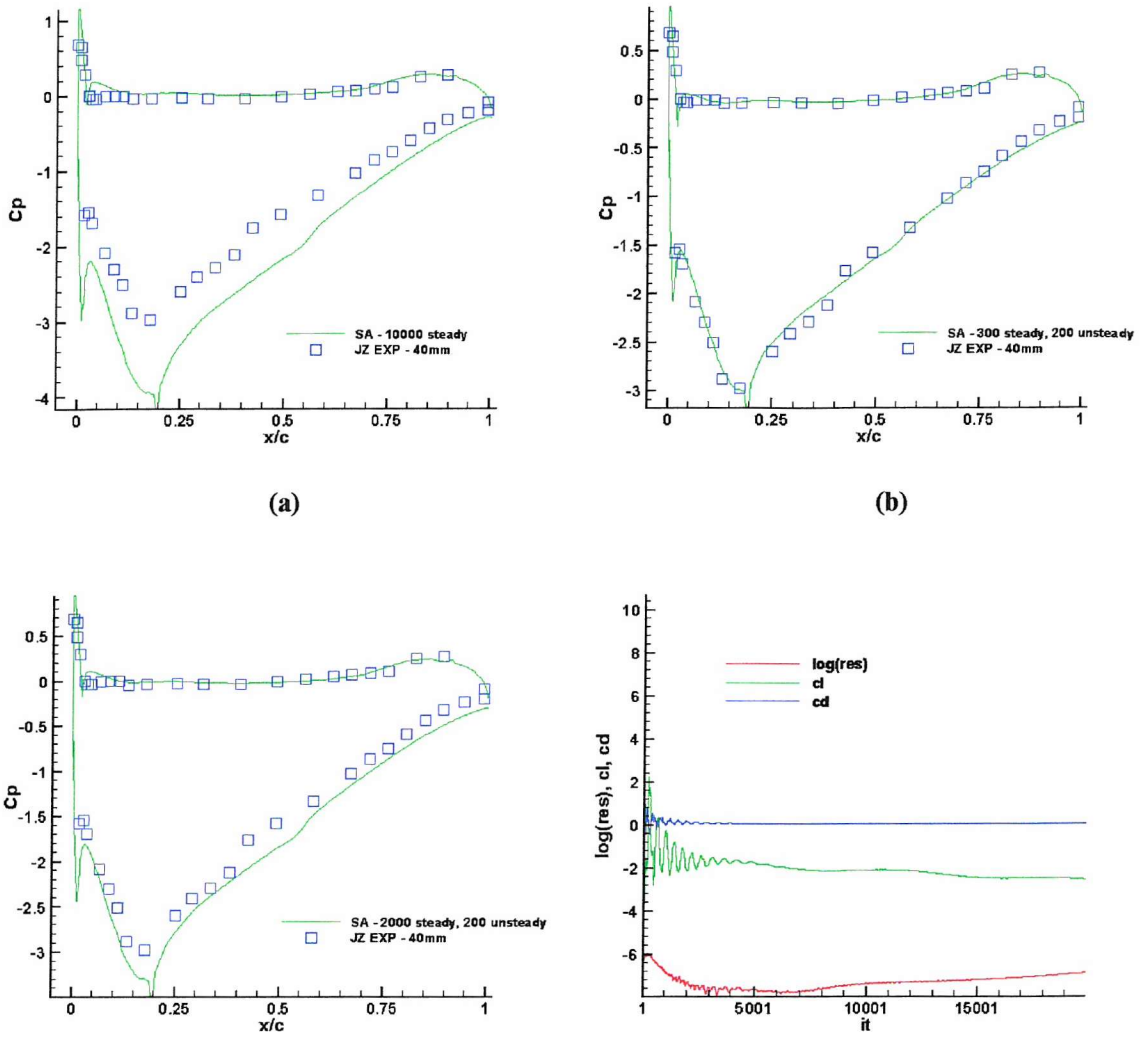

Figure 17. CFL3D Results: Plots representing simulations carried out on the Tyrell-26 airfoil at a ride height of 40mm, h/c=0.179 with 276, 285 grid points. Experimental results taken from Zerihan (JZ) (a) 10,000 Steady State Iterations, (b) 300 steady state and 200 unsteady state iterations, (c) 2000 steady state and 200 unsteady state iterations, (d) Histories of solution residual, Coefficients of Lift and Drag over a steady state simulation using 20,000 iterations.

The spikes at the leading edge shown in Fig.17 and all subsequent plots involving this geometry can be explained by discontinuities around the leading edge. The aerofoil was derived from a NASA GA(W)-2 LS(1)-0413 MOD profile as described in Chapter 2 (Fig.4). In doing this, small discontinuities were left at the leading edge as highlighted in Fig.18 by blue circles. The discontinuity on the pressure surface is much more noticeable than that on the suction surface.

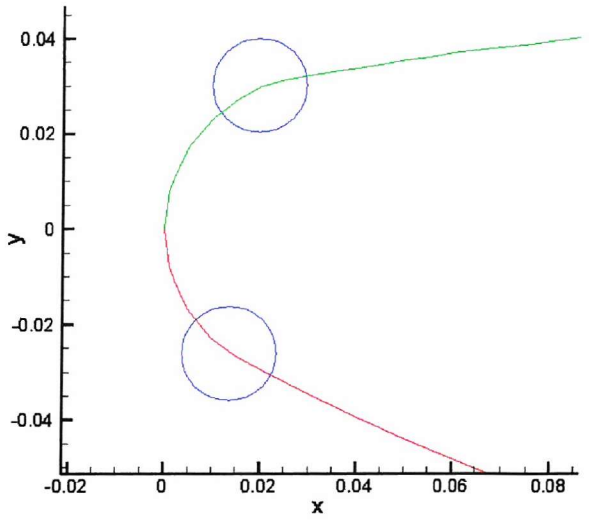

Figure 18. Highlighting discontinuity in Tyrell 026 aerofoil leading edge.

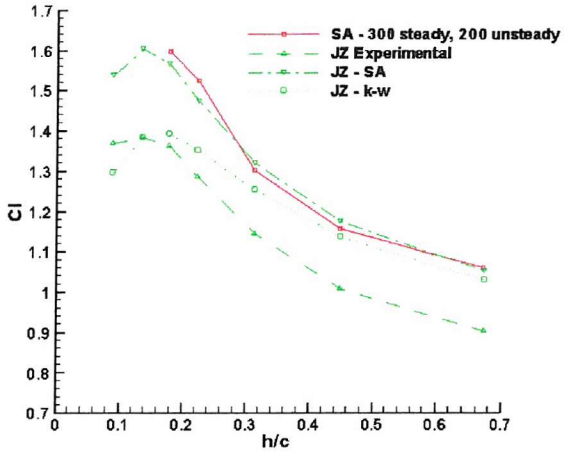

Figure 19. CFL3D Results: Coefficient of Lift plots taken from Zerihan (JZ) compared to the results from the cases with 300 steady and 200 unsteady iterations.

The time penalty to obtain steady state solutions was decided to be too great to continue the use of CFL3D. The uncertainty that these solutions were entirely converged especially if no experimental data is available for comparisons would made future work very difficult to defend. Due to these reasons the migration to Fluent was decided upon despite the large amount of time invested in CFL3D.

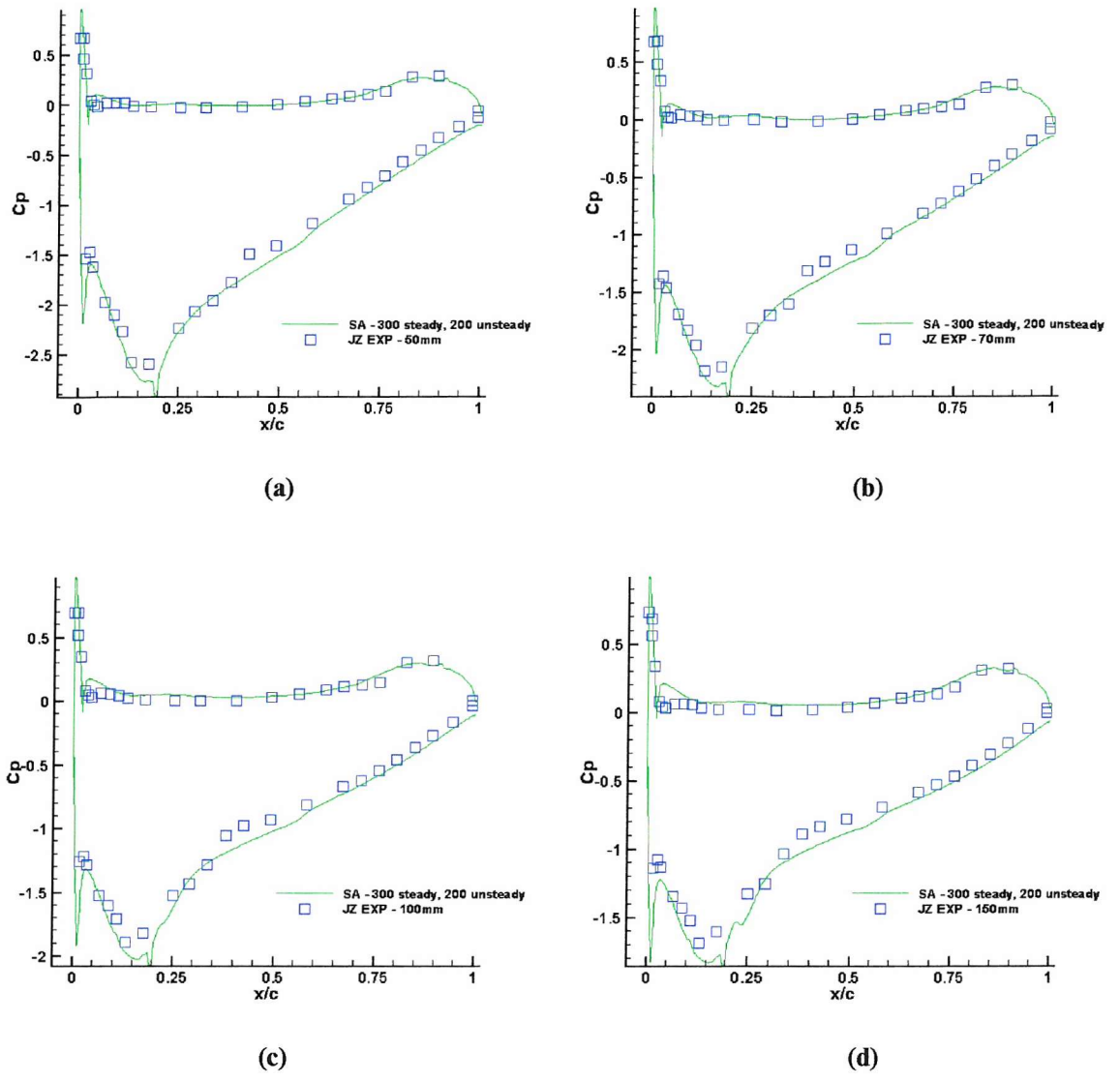

Figure 20. CFL3D Results using steady/unsteady strategy (300 and 200 steps respectively for each) with 276, 285 grid points at all heights: Coefficient of Pressure for heights (a) 50mm, h/c=0.224, (b) 70mm, h/c=0.313, (c) 100mm, h/c=0.448, (d) 150mm, h/c=0.671. Experimental results taken from Zerihan (JZ).

Following the preliminary free-stream and the two-dimensional wing in ground tests, it was found that the modelling of the wake for all these flows was extremely poor when using CFL3D. This was even the case when extremely dense grids were used. Figure 21, a plot of the Mach number of the wake when the aerofoil is close to the ground shows this clearly. The wake defect reduces more quickly than seen in Zerihan, an effect which is probably grid dependent. The grids were heavily altered in order to try to solve this problem, including adjusting the density and even the angle of the trailing edge grid region in order to follow exactly the expected path of the wake. Based on this and other factors, including the expectation of very long computational times for the three-dimensional DES cases, it was

decided that the best course of action would be to discontinue the use of CFL3D and to use a previously proven program for this geometry, namely Fluent (c.f. Devièse [34]).

Based upon the experience gained in grid development and with the availability of unstructured grids, it was felt that sufficient progress could be made using Fluent to complete the project. It would however require repeating the initial grid tests along with the two-dimensional test case results using the RANS turbulent models. These are required in order to allow direct comparison of models within the same package.

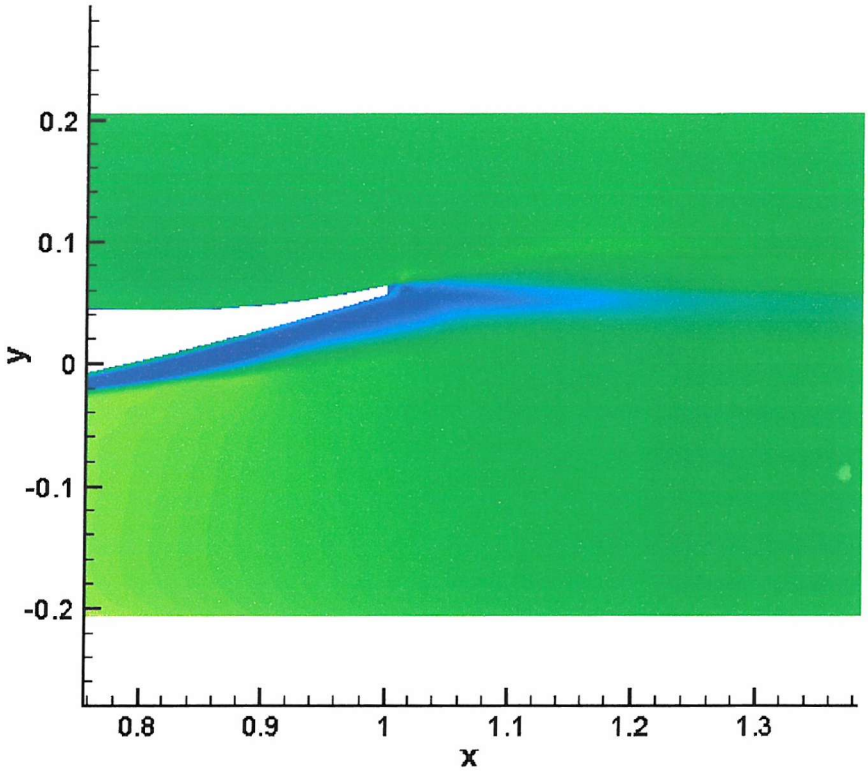

Figure 21. The Wake region showing a Mach number contour plot.

4.3 Fluent Results: NACA0012 and NACA4412

The NACA0012 and NACA4412 simulations as carried using the CFL3D code were repeated using Fluent. The same grids were used in order to see if the trailing edge accuracy issue was grid dependent or code dependent. The results shown in Fig.22 (NACA0012) and Fig.23 (NACA4412) illustrate that the accuracy obtained using Fluent is greatly improved. Therefore, we can conclude that the inaccuracies seen with the CFL3D solutions were an issue with the code and not the grids. This further establishes the use of Fluent as a reasonable decision in order to build confidence into future results.

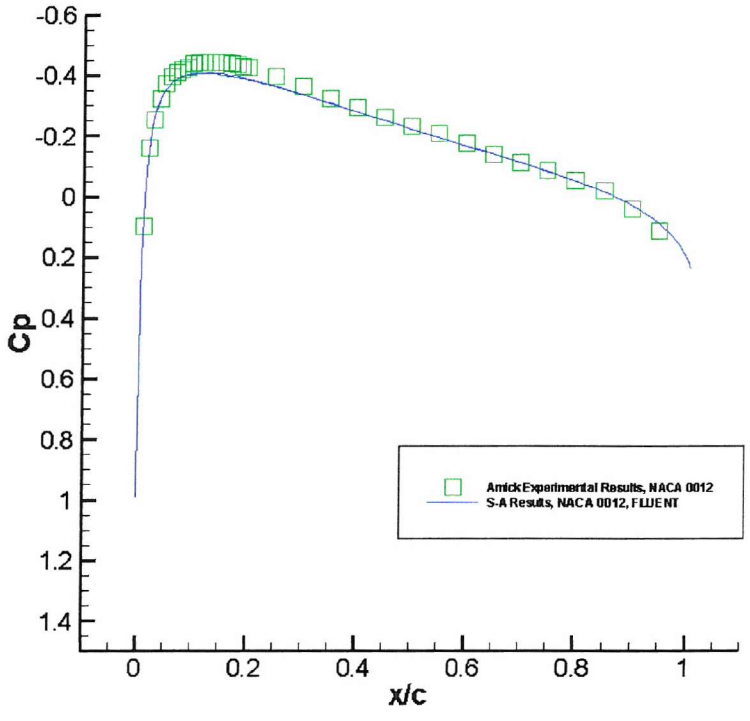

Figure 22. Fluent Results: Plot of Coefficient of Pressure against x/c for the grid type in Fig.7 on the NACA0012 airfoil at zero angle of attack with 36,864 grid points (as per Fig.13).

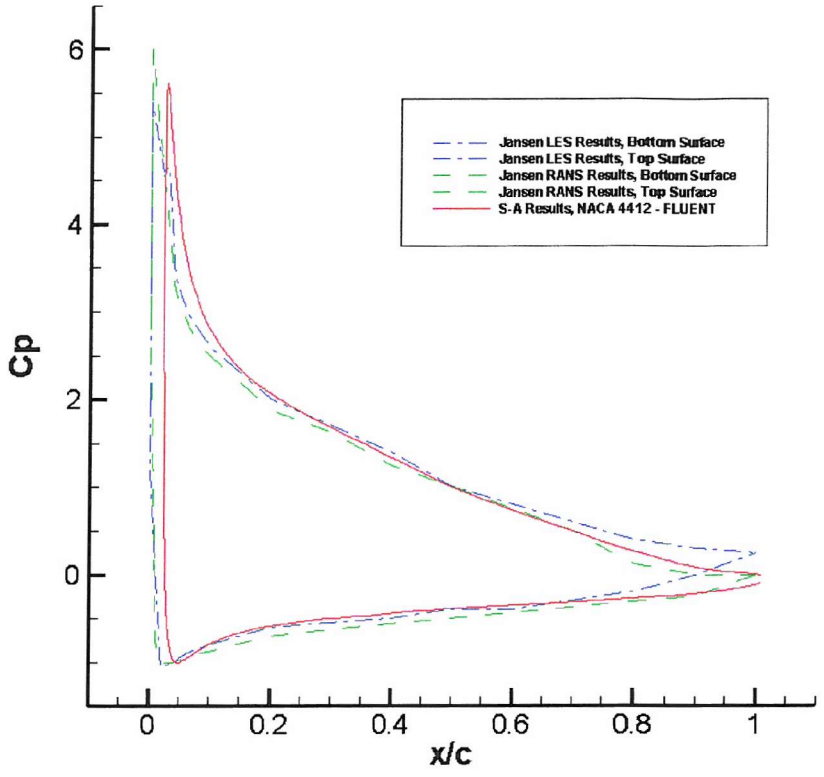

Figure 23. CFL3D Results: Plot of Coefficient of Pressure against x/c for the grid type in Fig.8 on the NACA4412 airfoil at 12° angle of attack with 36,864 grid points (as per Fig.16).

4.4 Fluent Results: Two-Dimensional Wing in Ground Effect Flows

The initial grid density of approximately 95,000 grid points using both structured and unstructured grid types was used as the validation case. This grid type was previously referred to as the standard grid and this grid type was the first to produce acceptable results without any anomalies appearing in the flow domain during the grid development. These anomalies can be caused by poor grid layout and/or poor grid distribution or too coarse a grid. This grid was not necessarily expected to be the smallest required to produce a reasonable solution, merely a first iteration.

The remaining grid densities were used in order to analyse the grid dependence and also the cost-benefit and accuracy trends of a finer or coarser grid.
These grids are run using the four RANS turbulence models stated earlier, and using the standard Fluent settings.

4.5 First Grid – Standard

Results using the first grid to produce a reasonable solution using Fluent are presented first. Grid point numbers are shown in Table 1. The grid contains a combination of structured and unstructured regions. The structured sections include a small C-type grid surrounding the airfoil and a second section along the ground. The rest of the domain is entirely unstructured. This remedies the stretching problems inherent in structured grids and also reduces the number of points used in certain areas. This is possible since an unstructured region does not have to be symmetric in the number of points used. In the upstream section where the structured ground region meets the unstructured region, the bottom of the unstructured region has the same points as the structured one, but the top of the unstructured area has significantly fewer points. This is allowable due to the lack of any fine-scale flow features in the area. This method is applied along the top of the domain also. The grid was tested over various heights from the ground to give a picture of the operation of the aerofoil in these circumstances and also to enable direct comparison with the experimental data of Zerihan.

4.6 Comparison Grids – Coarse and Fine

The coarse grid is identical to the standard grid apart from the coarser region applied in the aerofoil C-type grid section. It is referred to in plots as "coarse" to distinguish it from the "standard" grid results. Grid point numbers are shown in Table 1. The fine grid is also the same as the other two grids, except for the higher density of grid points within the aerofoil C-type grid section. This is referred to as the "fine" grid in plots. Points could have been added to all areas of the grid at this point. However, in order to keep the study focused, it was felt that clustering points in regions where no flow features would exist would not be overly beneficial at this point. The main focus of the analysis is on the surface of the aerofoil and therefore the region surrounding this is the most beneficial place to cluster points. This would then provide insight into the grid dependency of the results

4.7 Fluent – Grid Dependency and RANS Model Study

This section presents the results attained from the studies carried out over the various grids and RANS models. Figures 24, 25 and 26 show C_P plots for the heights 20mm, 30mm and 40mm respectively. Each plot shows results from the three grids for each of the RANS models and includes the experimental data of Zerihan. The grid sizes are presented in Table 1. The C-type section is varied in order to adjust the density of the grids. The coarse grid uses 201x41 points, the standard grid uses 401x81 points and the fine grid uses 601x121 points in this section. The k-ε and k-ω models do not perform very well in this geometry compared to the k-ωSST and the SA models.

The effect of convergence criteria in Fluent was checked. Figure 27 presents the results when the convergence criteria in Fluent were reduced by a factor of 10 for the 40mm grids using the SA model. A degree of increased accuracy is seen but this is coupled with an increase in time to reach a converged solution. The problem with the k- ε and k-ω models were not solved by changing the convergence criteria.

In the case of the k-ω plots for the ride height of 40mm (fig.26 b and e), it can be seen that drastically incorrect results are attained. The reason for this is unknown. We checked that there was no error in the input or any problems with the grid (which was the same one used for the other models). This highlights the manner in which the grid-dependence can be affected by the choice of a turbulence model. This has profound implications for our future simulations, in that one specific grid cannot be assumed to be universally valid for all models and geometries. It means that in order to acquire solutions which can be reliably compared to experimental results, separate grid-independency checks need to be performed for each RANS turbulence model, ride height and angle of attack. This also means that when using commercial computational packages for industries like motorsport and even the automobile industry in general, a degree of thoroughness is required when generating the necessary grids. This will of course add to the time and cost of the problem being solved.

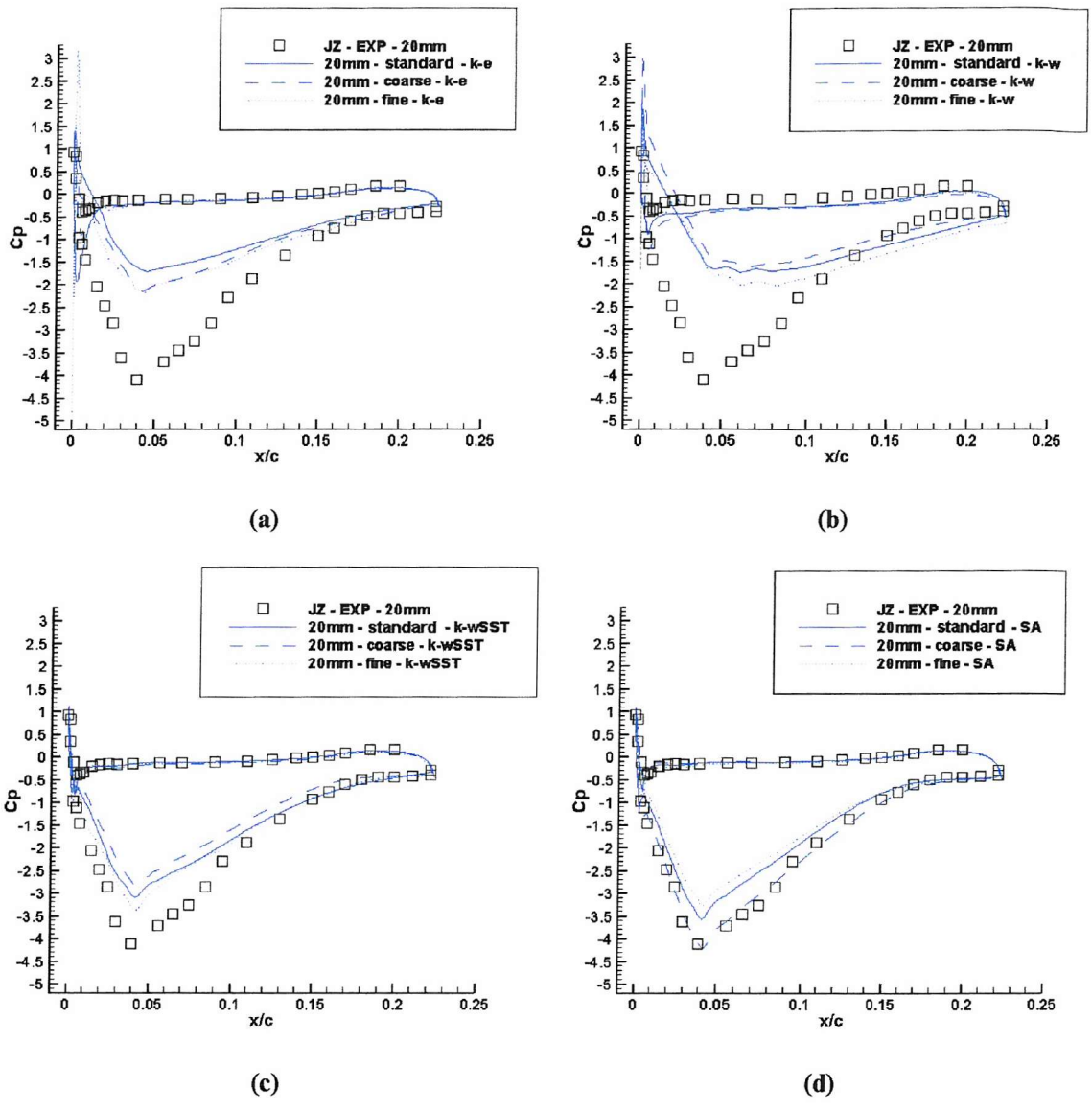

Figure 24 (a) to (d). C_P comparison plots for the 20mm height used with the RANS models in Fluent, based upon the default convergence set by Fluent. (a) k-ε model; (b) k-w model; (c) k-ωSST model; (d) SA model. Experimental results taken from Zerihan (JZ). Coarse = ~65000 points; Standard = ~95000 points; Fine = ~135000 points

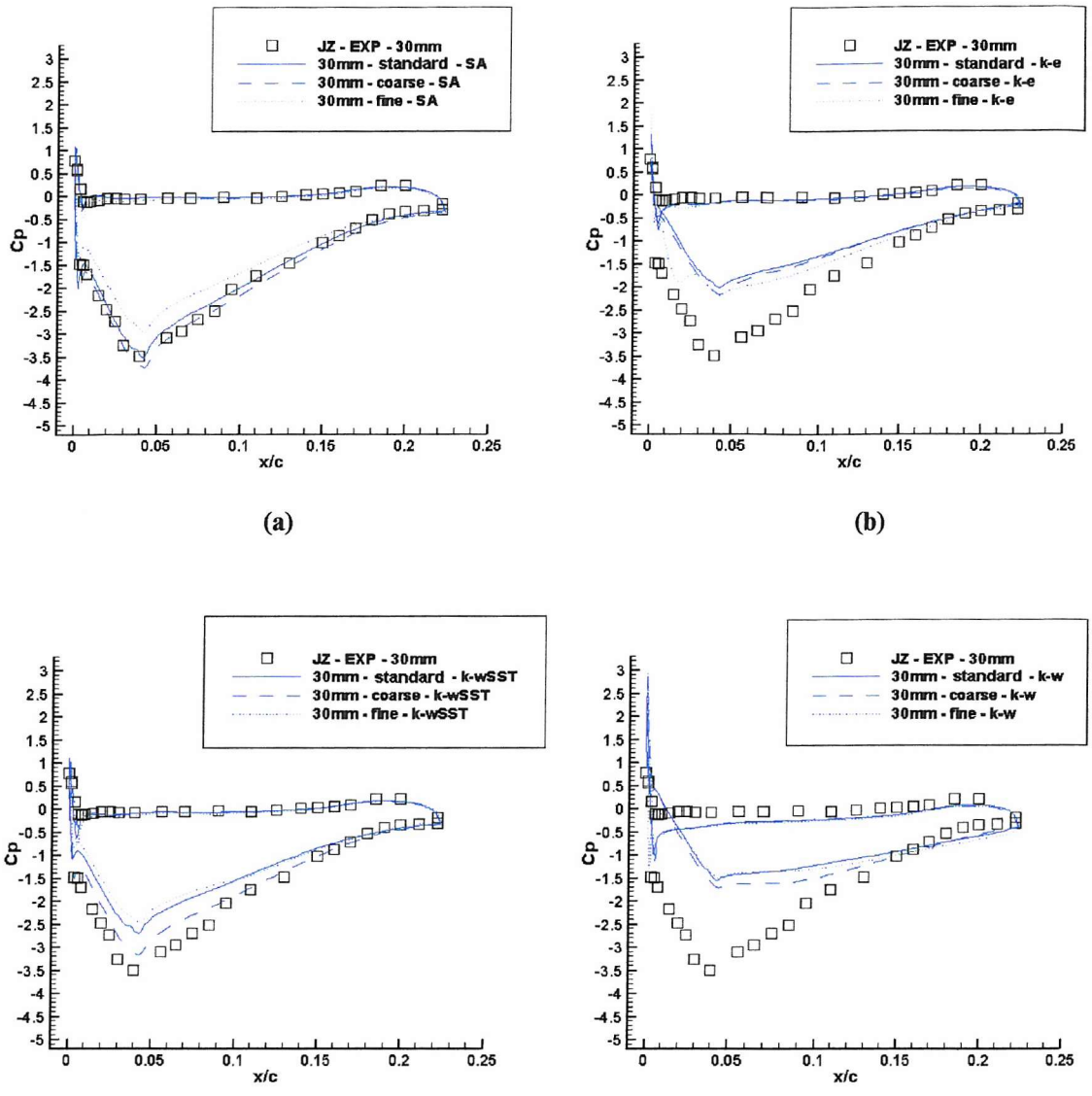

Figure 25 (a) to (d). C_P comparison plots for the 30mm height used with the RANS models in Fluent, based upon the default convergence set by Fluent. (a) k-ε model; (b) k-w model; (c) k-ωSST model; (d) SA model. Experimental results taken from Zerihan (JZ) Coarse = ~65000 points; Standard = ~95000 points; Fine = ~135000 points

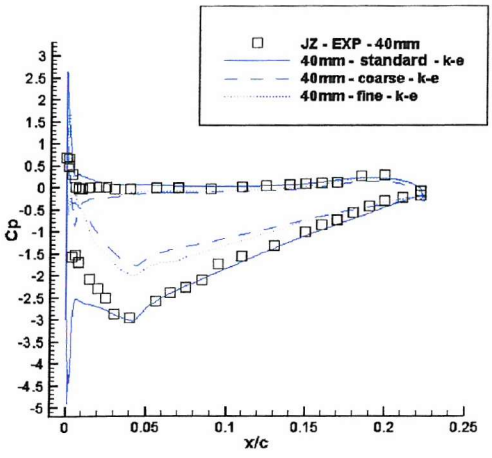

(a)

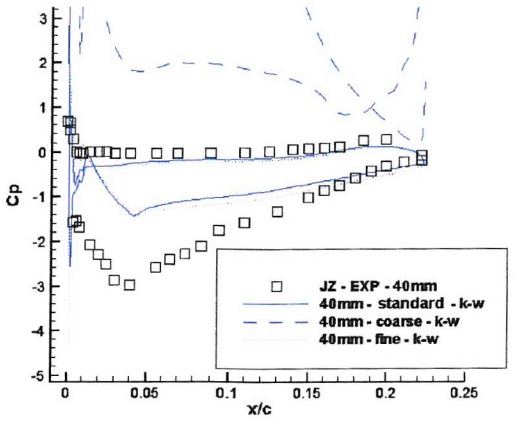

(b)

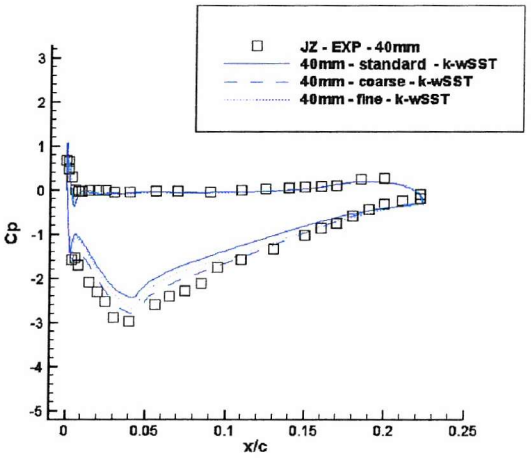

(c)

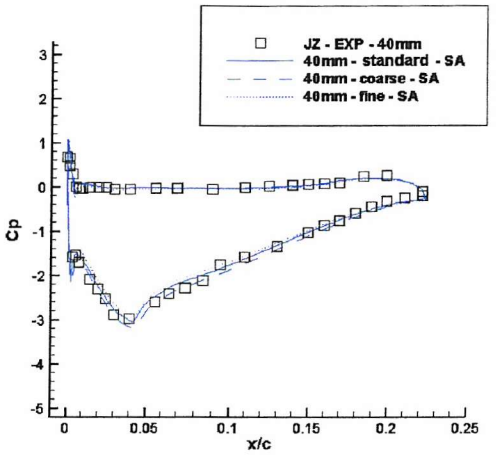

(d)

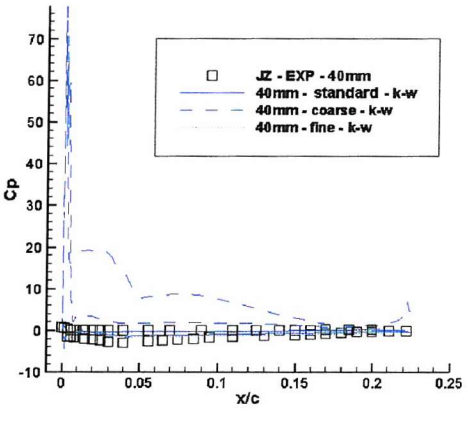

(e)

Figure 26 (a) to (e). C_P comparison plots for the 40mm height used with the RANS models in Fluent, based upon the default convergence set by Fluent. (a) k-ε model; (b) k-ω model; (c) k-ωSST model; (d) SA model; (e) Resized plot of the 40mm k-ω plot to show extent of coarse grid deviation. Experimental results taken from Zerihan (JZ) Coarse = ~65000 points; Standard = ~95000 points; Fine = ~135000 points

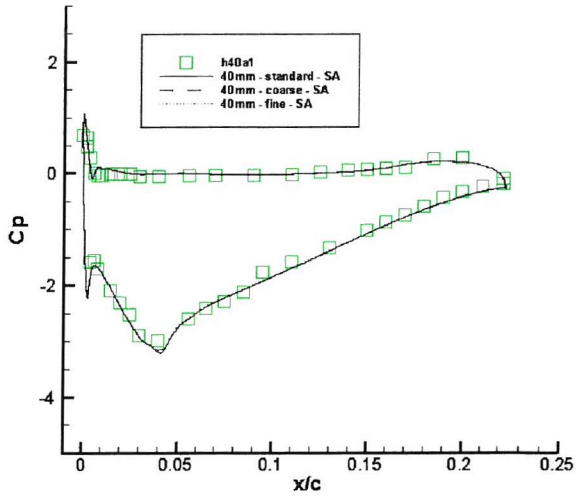

Figure 27. C_P comparison plots for the 40mm height used with the RANS models in Fluent, based upon a convergence set to a factor of 10 lower than the default set by Fluent. The SA model was used across all the grids. Experimental results taken from Zerihan (JZ)
Coarse = ~65000 points; Standard = ~95000 points; Fine = ~135000 points

Figure 28 shows C_P plots for the remaining heights on the standard grid. These show the continued pattern of the poor performance of the k-ε and k-ω models in comparison to the other models.

While the trailing edge and the upper-surface of the aerofoil are fairly well modelled in each case, the suction side peak is problematic for the k-ε and k-ω models. Likewise, there is a difference between the k-ωSST and the SA models in solving this region, with the SA model yielding the best result. The k-ωSST model under predicts by between 10 to 20% based on the peak C_P value on the suction surface.

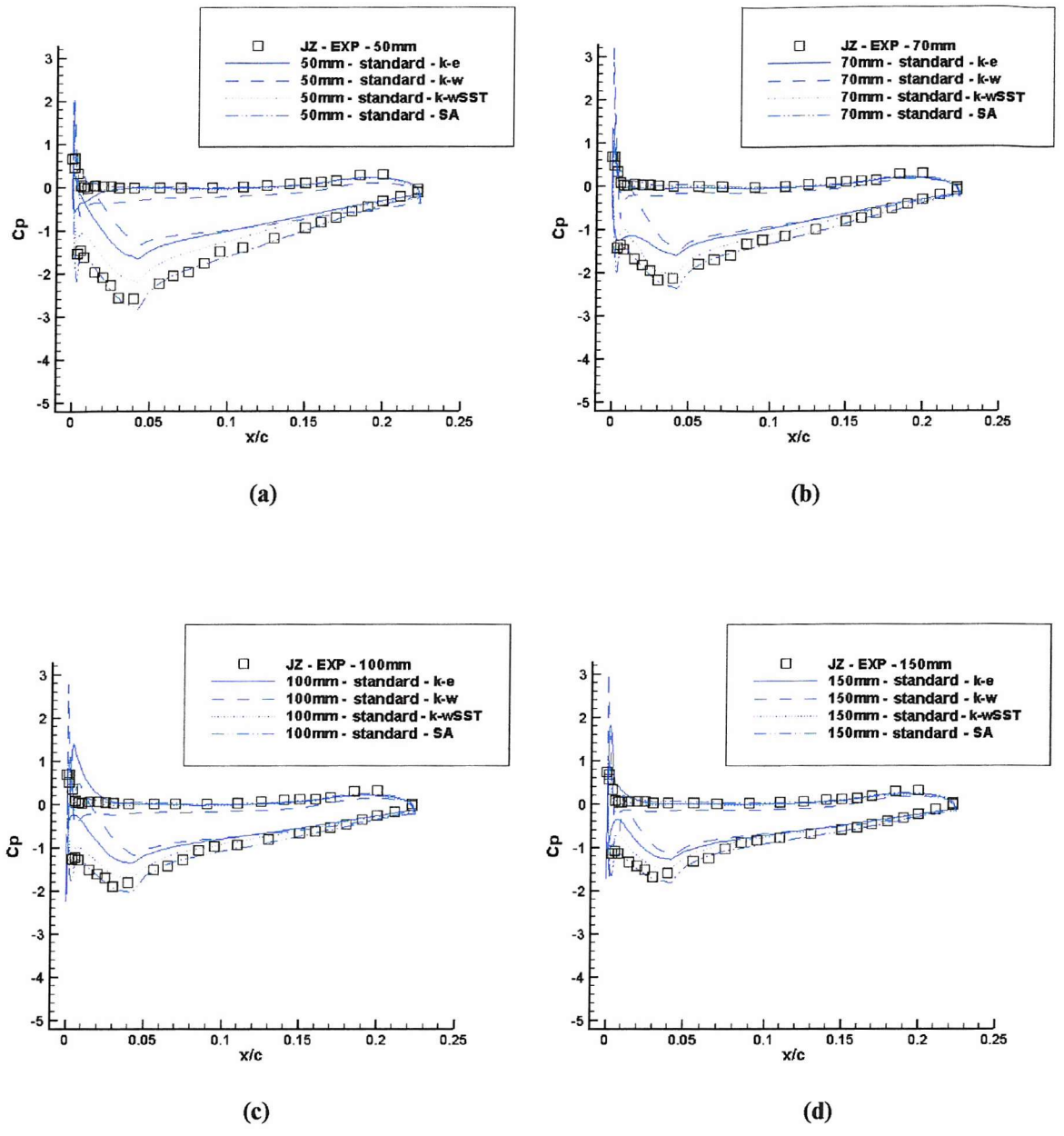

Figure 28 (a) to (d). C_P comparison plots for the 50mm, 70mm, 100mm and 150mm grids used with the RANS models in Fluent, based upon the default convergence set by Fluent. (a) 50mm Grids; (b) 70mm Grids; (c) 100mm Grids; (d) 150mm Grids. Coarse = ~65000 points; Standard = ~95000 points; Fine = ~135000 points

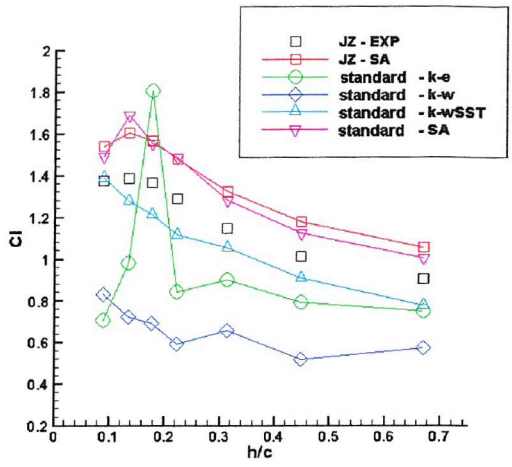

Figure 29. Plot showing the C_L on the Standard Grid for the Models used and based upon the default convergence specified by Fluent. Standard = ~95000 points

Presented in fig.29 is a plot of the net C_L values for the standard grid (the C_L values have been made positive for ease of visualisation). These results in general adhere to the expected pattern of gradual increase in downforce as the wing approaches the ground, then the short plateau region followed by a sudden drop in downforce. This is consistent with the experimental and preliminary computational data (SA model, using the CFL3D package) of Zerihan. Also noteworthy is the close agreement between the SA Zerihan results and the present Fluent/SA results. The large variation can be explained by the different grids and computational packages used. Zerihan used an entirely structured grid consisting of many blocks with approximately 35,000 points. He also used the CFL3D package under the conditions detailed earlier. As illustrated in fig.30, the Coefficient of Drag plots also show the difference in accuracy of the models. While the only comparison data available was a computational simulation carried out by Zerihan, this is enough to confirm the point. As this data comes from the same simulations used for his C_L plots, we adopt it for the C_D comparison. While the k-ε and k-ω solutions again differ greatly and have large deviations from the experimental pattern, the k-ωSST and the SA models present reasonable results. Figure 30 (b), (c) and (d) show the output from the three grids used, and it can be seen that no significant quantitative difference is present.

For C_L , the k-ωSST model agrees closest with the Zerihan baseline. This, along with the SA model, is the only of the four which perform with any reliable accuracy and consistency. The k-ωSST model however, fails to pick up the presence of the downforce plateau and sudden drop close to the ground exhibited in the C_L plots. This could be down to the short Fluent convergence time.

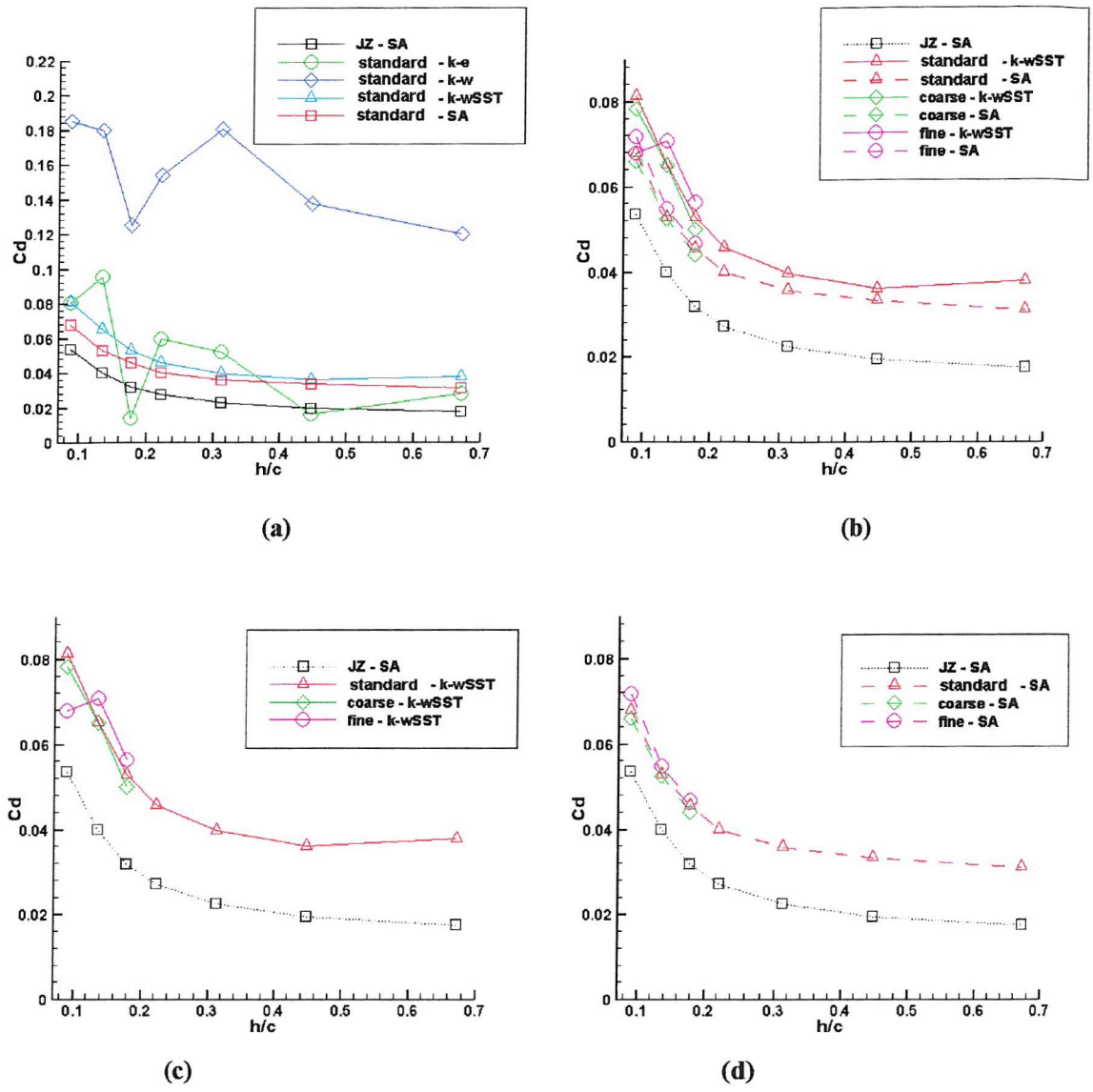

Figure 30. Coefficient of Drag Plots for the various ride heights based on (a) All models on the standard grid; (b) Comparison of the k-ωSST and SA models on the three grids; (c) Detailed plot of the SA model on all three grids; (d) Detailed plot of the k-ωSST model on all three grids. Coarse = ~65000 points; Standard = ~95000 points; Fine = ~135000 points

These results only represent the in-built Fluent convergence criteria which specifies a net value of 10^{-3} in regard to the velocity change over successive iterations. There is also the possibility of manually prescribing the convergence criteria or to run without any such criteria. This is useful in that it allows for the investigation of very long simulations to be completed. The reason for this stems from the problems encountered with CFL3D. When very long simulations were run, it was discovered that the solution appeared to converge but later drastically diverged and eventually went into a pseudo-unsteady state as described earlier. The ability to allow a simulation to run indefinitely means this previous problem can be shown to be non-existent in Fluent.

However, from an overview of the results, as pointed out in Chapter 1, the models used here have performed very much as expected. The models as evaluated by Bardina et al [28] were ranked with the k-ωSST and SA models showing the best performance and the k-ε and k-ω models showing poor performance in numerous cases including complex geometries and flow-fields. This behaviour has been found here. The best performing model in this case is again the k-ωSST model, shown by the C_L values in fig.31. The SA model is the next most accurate; it over-estimates the C_L, but provides the best agreement with the overall C_L profile. Some computational costings were carried out which included calculating the duration to compute a set number of iterations. In the case of the SA model, it performed a set number of iterations 1.68 times faster than the k-wSST for the same grid. However, the SA model required on average four to five times more iterations to converge under the same conditions as the k-wSST model. Coupling this with the speed per iteration, the k-wSST model was found to be approximately 2.5 times faster than the SA model. The k-ε model is less accurate, with some rather spurious results. The standard k-ω model is the least accurate.

4.8 Fluent – Flowfield Physics, SA Results

By studying the flowfield a clearer image of the physics involved in wing in ground effect flows can be obtained.

Figures 31 and 32 show the pathlines and velocity contour flow-fields for the 20mm and 150mm ride height results respectively (plots for the remaining heights are presented in Appendix A, fig. 35 to 39). The separation region for h = 20mm is illustrated in the Velocity Magnitude(m/s) plot by an area of decreased velocity. When compared to the h = 150mm results, this demonstrates the effect of placing the aerofoil closer to the ground. By examining this and the other Velocity Magnitude plots for all the ride heights in conjunction with the velocity flood plots, the maximum velocity close to the front of the suction surface is seen to vary. This velocity for the 150mm ride height is approximately 47.6m/s whereas for the 20mm ride height it is about 62.1m/s. This shows that there will be a greater reduction of pressure over the suction surface for the 20mm case compared to the 150mm case. This pattern is consistent throughout the studies performed.

This is reflected in both the Static Pressure and Coefficient of Pressure (C_P) contours. The approximate minimum C_P value for the 150mm case is -1.8 while the corresponding value for the 20mm case is -3.57. The expected reduction in pressure is indeed present. The point of maximum velocity also as expected coincides with the point of minimum pressure.

The wake from the aerofoil increases as the ride height is reduced. This is shown in the Velocity Magnitude plots by a region of low velocity downstream of the trailing edge. The wake is quite small and confined in the 150mm case and develops into a large region encompassing a portion of the suction surface in the 20mm case.

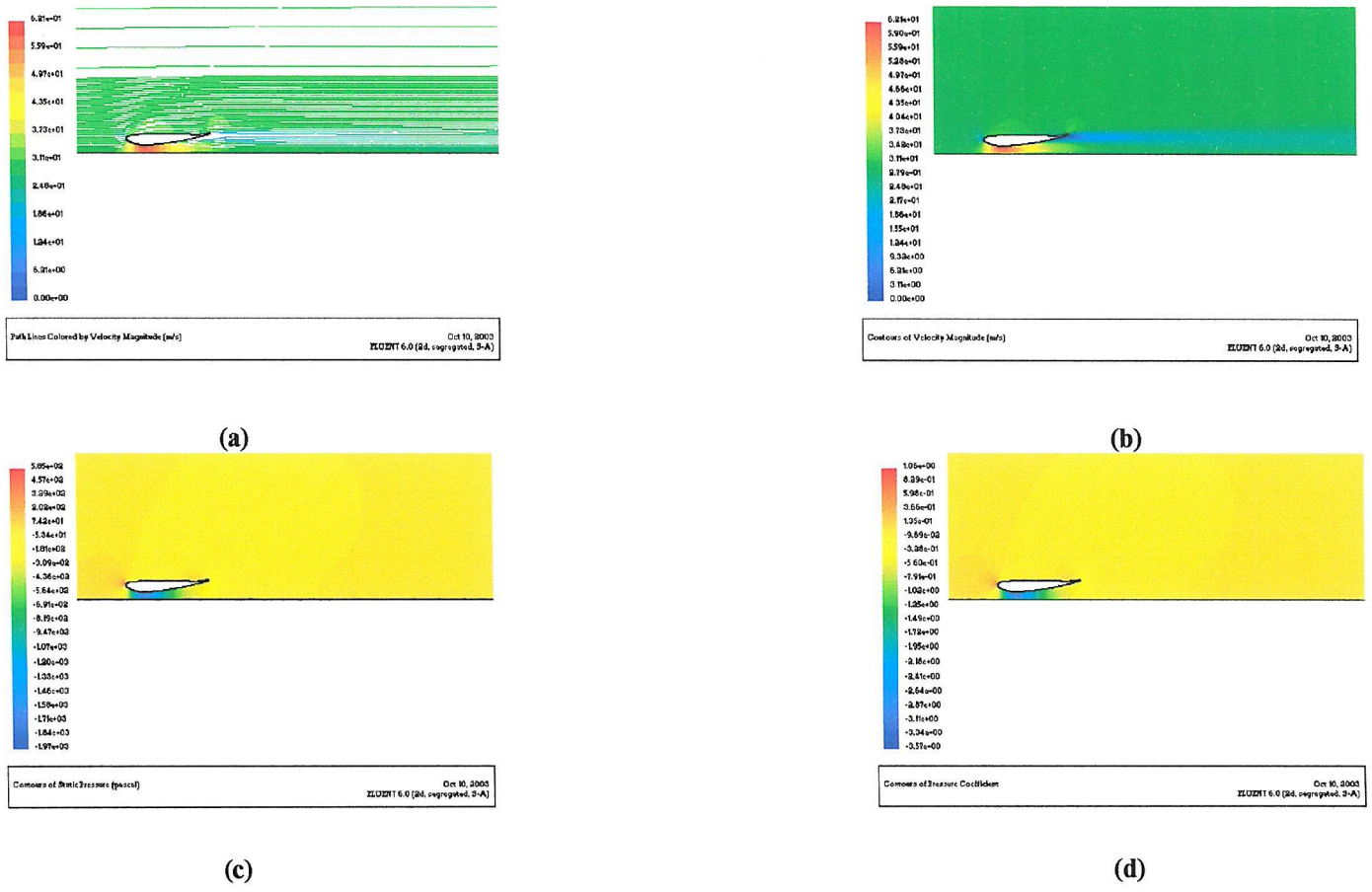

Figure 31. Fluent Results, 20mm Ride Height (a) Velocity Contour Plot; (b) Velocity Flood Plot; (c) Static Pressure Flood Plot; (d) Coefficient of Pressure (C_P) Flood Plot.

The three-dimensional effects, as discussed earlier, are assumed to be minimal along the spanwise symmetry line or centre of the wing, and so the wake shown is assumed to be correct. However, downstream of the trailing edge, the wake could be affected by three-dimensional flow structures such as trailing vortices shed from the wing tips.

By examining the suction surface on the Static Pressure plots, the low pressure region for the 150mm case encompasses almost the entirety of the lower surface. However, by looking at the remaining cases up to the 20mm case, the low pressure region becomes more localised. This appears to be directly caused by the proximity of the ground. While it may be expected that an increase in velocity is observed, it does not follow that this increase has an effect on a larger area of the suction surface. The presence of the ground causes large separation from the suction surface. This separation is shown in the Velocity plots. The separation encroaches on the area of low pressure and so reduces the region it has an effect upon. This increasingly large region of separation ties in with the diffuser theory whereby the smaller the gap between the wing and the ground the greater the effect on the flow. Hence the pressure drop, the velocity increase and downforce gain. Results shown by Zerihan, which show a sudden drop off in downforce, can therefore be explained by this. The closer the wing is to the ground the higher the velocity and so the greater the downforce. However, a point is reached whereby the flow through this section is restricted, as with any contraction. This is especially prevalent here as the air will disperse around or over the wing as opposed to under the suction surface. This will then reduce any downforce present.

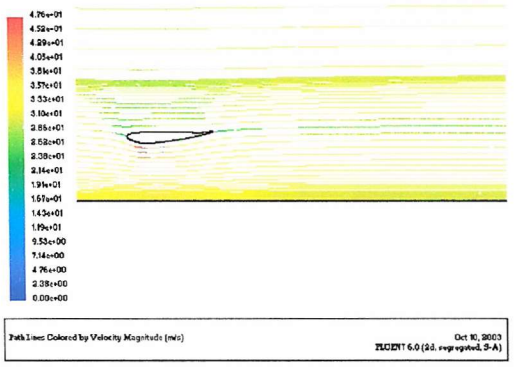

(a)

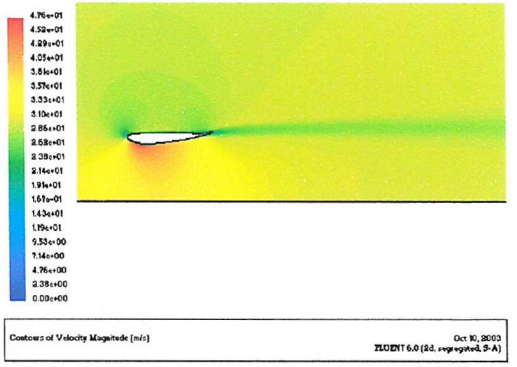

(b)

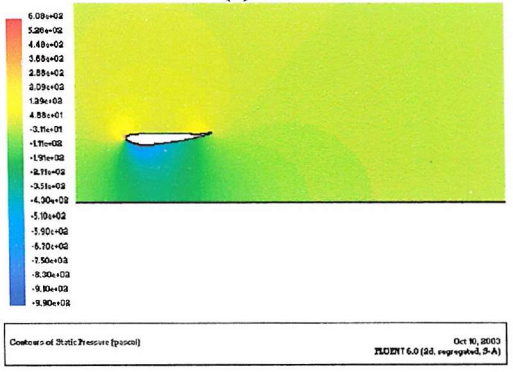

(c)

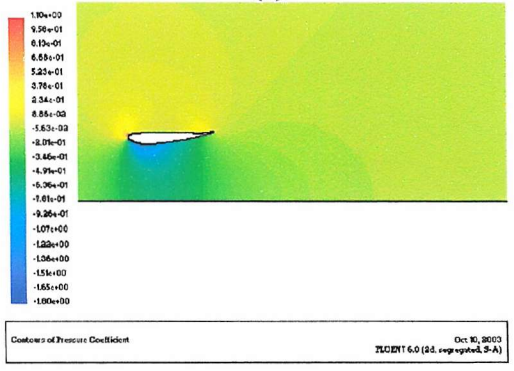

(d)

Figure 32. Fluent Results, 150mm Ride Height (a) Velocity Contour Plot; (b) Velocity Flood Plot; Static Pressure Flood Plot; (d) Coefficient of Pressure (C_P) Flood Plot.

4.9 Unsteady RANS

Two-dimensional Unsteady RANS (URANS) simulations were carried out using the same grids as used for the steady-state RANS simulations. These were used in Fluent with the SA model. Various time-steps and convergence criteria were trialled with no success. These were also carried out using the various ride heights. The grids used all converged into a steady-state solution. It was believed that a lack of grid density caused this, so further simulations were carried out with significantly finer grids in the region of 500,000 points. The simulations did not produce any unsteady solutions.

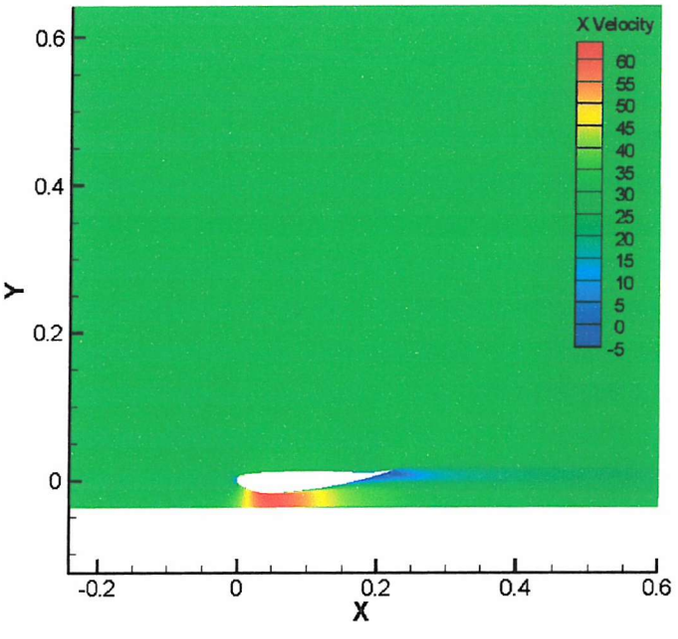

Figure 33 A flood plot of X-Velocity using URANS with a time step of 0.001 on a ride height of 20mm.

A typical X-velocity flood plot and Lift and Drag plots are presented (fig 33 and 34) which show that the solution converges after quite a short period of time. The example shown is with the aerofoil at a ride height of 20mm and a time step of 0.001.

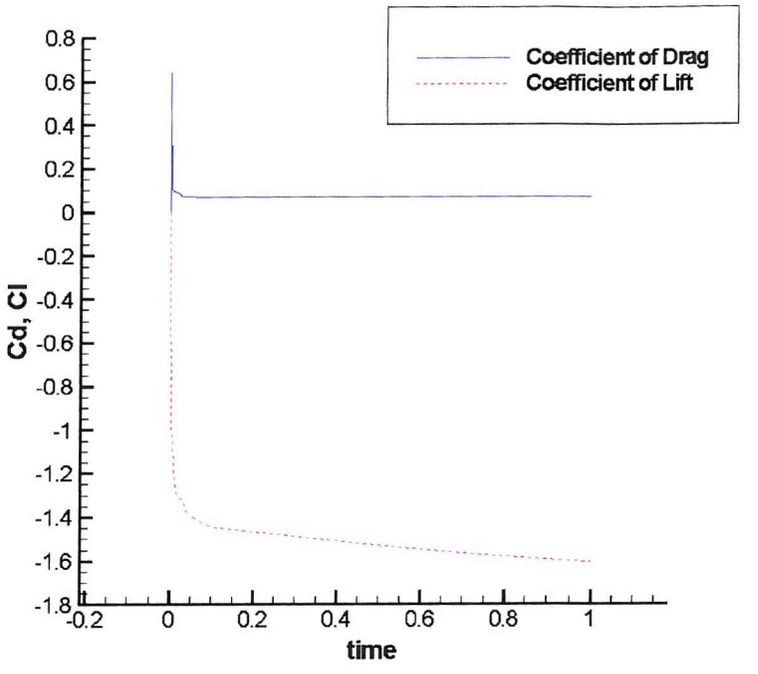

Figure 34 A plot of C_D and C_L using URANS with a time step of 0.001 on a ride height of 20mm.

Following this, and based upon observations made by Devièse [34]. During his study of LES on a wing in ground effect he was unable to obtain a result from Fluent using URANS. He was however more successful using LES. Due to this observation and experience with Fluent in this study, it was decided that there is no further value in pursuing the approach of URANS using Fluent.

An attempt was made to further the project by trying to run a three-dimensional DES simulation. However, with the lack of results from the URANS simulations, very little experience could be applied to the DES problems. Adding to that the time constraints of this project, any further investigation of the performance of DES using a wing in ground effect could not be progressed.

Chapter 5

Conclusions and Recommendations for Future Work

5.1 Conclusions

A two-dimensional CFD study of a Wing/Aerofoil in Ground Effect has been completed. This was carried out utilising two computational packages, CFL3D (v.5) and Fluent (v.6). The combination of these packages enabled the deeper understanding of the shortcomings of CFD packages, the development of grids and the requirements for accurate output. The effect of using different RANS turbulence models on the same grids along with the effect of varying the grid densities were also considered.

The results and conclusions made by Zerihan based upon his experimental single element work are vindicated in this project. This also reversely validates the computational work in this project. The results from the CFL3D study show that the best grid layout entails a C-type block encircling the aerofoil or wing. This however causes grid stretching problems which are very serious when using structured grids. In order to overcome the stretching of structured grids, heavy modification coupled with a large increase in grid point counts is required. Compressible flow solvers are shown to be unsuitable for incompressible flow without some possible quick fixes as detailed by Zerihan which are very expensive compared to the standard computational methods. Using unstructured grids overcomes all of the stretching problems in grids using C-type blocks while also greatly reducing the need for large numbers of grid points.

Results using Fluent show that variations in grid density do affect the accuracy of the results and that this is not a linear relationship. However, this should be studied further by making the convergence criteria more stringent. The best performing models were the k-ωSST and the SA models with the k-ε and k-ω models performing poorly when compared to the experimental results of Zerihan.

URANS simulations proved unsuccessful despite much investment of time. Many variable alternates were trialled but as with conclusions by Devièse [34], the URANS performance of Fluent with this geometry showed no signs of producing accurate results.

DES simulations were also attempted with no results achieved due to time constraints. However, the inclusion of DES in the latest version of Fluent (v6.1) will allow for future investigations of its performance using a wing in ground effect.

5.2 Recommendations for Future Work

The results presented here pose some interesting questions as well as providing a very useful platform for some exciting development work.

- The effect of grid density on the accuracy of the results provides a potentially interesting area of further research. This could be combined with developing other grid layouts and also comparing to fully unstructured grids.
- The two-dimensional results provide a base for further study into three-dimensional computational tests but further work on the grid dependency could prove very interesting.
- Unsteady two-dimensional and three-dimensional simulations would provide a very interesting comparison to experimental results.
- The utilisation of the new in-built DES option in Fluent will provide a readily available and tested method of running this geometry under these conditions and thereby pushing the research of a wing in ground effect using computational methods forward. As this research using DES is only carried out under three-dimensionality, the physics of the wing in ground effect can be studied in even more detail. This also provides the necessary selling point that DES is no longer a research tool and that it is in a format already used by many in industry today.

Bibliography

[1] Katz, J. New Directions In Race Car Aerodynamics: Designing for Speed, Bentley Publishers, 1995.

[2] Agathangelou, B. and Gascoyne, M. Aerodynamic considerations of a Formula 1 racing car, SAE Publication 980399, 1998.

[3] Jeffrey, D. and Alperin, M. Aspects of the Aerodynamics of Year 2000 Formula One Racing Cars. 3rd Mira International Vehicle Aerodynamics Conference, Rugby, 18/19 October 2000.

[4] Ranzenbach, R. and Barlow, J.B. Two-dimensional airfoil in ground effect, and experimental and computational study, SAE Publication 942509, 1994.

[5] Ranzenbach, R. and Barlow, J.B. Cambered airfoil in ground effect, An experimental and computational study, SAE Publication 960909, 1996.

[6] Ranzenbach, R., Barlow, J.B. and Diaz, R.H. Multi-element airfoil in ground effect – an experimental and computational study, AIAA Paper 97-2238, 1997.

[7] Jasinski, W.J. and Selig, M.S. Experimental study of open-wheel race-car front wings, SAE Publication 983042, 1998.

[8] Knowles, K., Donahue, D.T. and Finnis, M.V. A study of wings in ground effect, 1994. Loughborough University Conference on Vehicle Aerodynamics, pp. 22.1-22.13.

[9] Zerihan, J. An Investigation into Aerodynamics of Wings in Ground Effect, PhD Thesis, University of Southampton, April 2001.

[10] Ranzenbach, R. and Barlow, J.B. Cambered airfoil in ground effect – wind tunnel and road combinations, AIAA Paper 95-1909, 1995.

[11] Raymond, A.E. Ground Influence on Aerofoils, Massachusetts Institute of Technology, NACA-TN-67, December 1921.

[12] Recant, I.G. Wind-tunnel investigation of ground effect on wings with flaps. Technical Report NASA-TN-705, NACA, May 1939.

[13] Kirkpatrick, D.L.I Experimental investigation of the ground effect on the subsonic longitudinal characteristics of a delta wing of aspect ratio 1.616. Technical Report 66179, Royal Aircraft Establishment, June 1966.

[14] East, L.F. The measurement of ground effect using a fixed ground board in a wind tunnel, Technical Report 70123, Royal Aircraft Establishment, July 1970.

[15] Klemin, A. A belt method of representing the ground. Journal of the Aeronautical Sciences, 1:198-199, 1934.

[16] Dominy, R., Aerodynamics of Grand Prix cars. Proceedings of the Institution of Mechanical Engineers, Part D: Journal of Automobile Engineering, 206:267-274, 1992.

[17] Spalart, P. R. and Allmaras, S. R., "A One-Equation Turbulence Model for Aerodynamic Flows", La Recherche Aerospatiale, 1:5-12, 1994.

[18] Shur, M., Spalart, P. R., Strelets, M., and Travin, A., "Detached-eddy simulation of an airfoil at high angle of attack". In: Rodi, W. and Lawerence, D. (eds.) 4th Int. Symp. Eng. Turb. Modelling and Measurements, Corsica, Elsevier, Amsterdam, pp. 669-678. May 24-24, 1999.

[19] Klausmeyer, S. M., Lin, J. C., "Comparative Results From a CFD Challenge Over a 2D Three-Element High-Lift Airfoil", NASA, Langley Research Center, Hampton, Virginia 23681-0001, NASA Technical Memorandum 112858, May 1997.

[20] Wilcox, D. C., "Turbulence Modelling for CFD", Second Edition, DCW Industries, Inc., 2000.

[21] Jones, W. P., and Launder, B. E., "The Prediction of Laminarization with a Two-Equation Model of Turbulence", International Journal of Heat and Mass Transfer, 15:301-314, 1972.

[22] Launder, B. E., and Sharma, B. I., "Application of the Energy Dissipation Model of Turbulence to the Calculation of Flow Near a Spinning Disc", Letters in Heat and Mass Transfer, 1(2):131-138, 1974.

[23] Wilcox, D. C., "Reassessment of the Scale-Determining Equation for Advance Turbulence Models", AIAA J., 26(11):1299-1310, Nov. 1988.

[24] Menter, F. R., "Two-Equation Eddy Viscosity Turbulence Models for Engineering Applications", AIAA J., 32:1299-1310, Nov. 1994.

[25] Menter, F. R., "Influence of Freestream Values on k-ω Turbulence Model Predictions", AIAA J., 30(6):1657-1659, June 1992.

[26] Menter, F. R., "Zonal Two-Equation k-ω Turbulence Models for Aerodynamic Flows", AIAA Paper 93-2906, Orlando, Fla., 1993.

[27] Menter, F. R. and Rumsey, L. C., "Assessment of Two-Equation Turbulence Models for Transonic Flows", AIAA Paper 94-2343, 25th AIAA Fluid Dynamics Conference, Colorado Springs, Colo., June 20-23, 1994.

[28] Bardina, J.E., Huang, P.G. and Coakley, T.J. Turbulence Modeling Validation, Testing, and Development. NASA Technical Memorandum 110446, April 1997.

[29] Pointwise Inc. Gridgen User Manual, Version 13.

[30] Amick, J. L., "Comparison of the Experimental Pressure Distribution on a NACA 0012 Profile at High Speeds with that Calculated by the Relaxation Method", Langley Aeronautical Laboratory, Langley Air Force Base, Va., August 1950.

[31] Jansen, K., "Preliminary large-eddy simulations of flow around a NACA 4412 airfoil using unstructured grids", Center for Turbulence Research, Annual Research Briefs, 1995.

[32] Jansen, K., "Large-eddy simulation of flow around a NACA 4412 airfoil using unstructured grids", Center for Turbulence Research, Annual Research Briefs, 1996.

[33] Milholen, W.E. Chokani, N. and Al-Saadi, J. Performance of three-dimensional compressible Navier-Stokes codes at low Mach numbers. AIAA Journal, 34(7):1356-1362, July 1996.

[34] Devièse, M. Aerodynamics of Single Wing in Ground Effect: Model Tests and CFD Simulations. MSc Thesis, School of Engineering Sciences, Aeronautics and Astronautics, University of Southampton, January 2002.

[35] Nikitin, N. V., Ficoud, F., Wasistho, B., Squires, K. D. and Spalart, P. R., "An Approach to wall modelling in large-eddy simulations", Physics of Fluids, 12(7):1629-1632, July 2000.

[36] Spalart, P. R. and Allmaras, S. R., "A One-Equation Turbulence Model for Aerodynamic Flows", AIAA Paper 92-0439, 1992.

[37] Spalart, P. R., Jou, W-H., Strelets, M., and Allmaras, S. R., "Comments on the feasibility of LES for wings, and on a hybrid RANS/LES approach", 1st AFSOR Int. Conf. On DNS/LES, Ruston, LA. In Advances in DNS/LES, C. Liu & Z. Liu Eds., Greyden Press, Columbus,OH, Aug.4-8, 1997.

[38] Travin, A., Shur, M., Strelets, M., and Spalart, P.R., "Detached-eddy simulations past a circular cylinder", Int. Journal of Flow, Turbulence and Combustion, 2000, 63(1-4):293-313.

[39] Strelets, M., "Detached Eddy Simulation of Massively Separated Flows", 39th AIAA Aerospace Sciences Meeting and Exhibit, Reno, NV, 2001-0879, January 8-11, 2001.

[40] Hedges, L. S., Travin, A., Spalart, P. R., "Detached-Eddy Simulations Over a Simplified Landing Gear", Journal of Fluids Engineering, vol. 124/1, June 2002.

[41] Krist, S. L., Biedron, R. T., Rumsey, C. L., "CFL3D User's Manual (Version 5.0)", First Edition, The Aerodynamic and Acoustic Methods Branch of The NASA Langley Research Center, Hampton, VA, USA, November 1996.

[42] Fluent Inc. Fluent User Manual, Version 6.0.

[43] Cokljat, D., Liu, F., "DES of Turbulent Flow over an Airfoil at High Incidence", 40th Aerospace Sciences Meeting & Exhibit, Reno, Nevada, 14-17 January 2002.

[44] Kim, C. S., Kim, C., Rho, O. H., "Parallel Computations of High-Lift Airfoil Flows Using Two-Equation Turbulence Models", AIAA Journal, Vol. 38, No. 8, 2000, pp. 1360-1368.

[45] Godin, P., Zingg, D. W., "High-Lift Aerodynamic Computations with One- and Two-Equation Turbulence Models", AIAA Journal, Vol. 35, No. 2, 1997, pp. 237-243.

Appendix

Suction Surface		Pressure Surface	
x/c	y/c	x/c	y/c
0.0000	0.0000	0.0000	0.0000
0.0010	-0.0076	0.0010	0.0079
0.0020	-0.0107	0.0020	0.0109
0.0049	-0.0168	0.0051	0.0173
0.0099	-0.0228	0.0101	0.0232
0.0149	-0.0266	0.0151	0.0271
0.0199	-0.0294	0.0201	0.0300
0.0249	-0.0320	0.0251	0.0313
0.0298	-0.0345	0.0301	0.0322
0.0348	-0.0369	0.0351	0.0330
0.0398	-0.0393	0.0401	0.0338
0.0448	-0.0416	0.0451	0.0346
0.0498	-0.0438	0.0501	0.0354
0.0548	-0.0460	0.0551	0.0361
0.0598	-0.0481	0.0601	0.0369
0.0698	-0.0520	0.0701	0.0382
0.0797	-0.0557	0.0801	0.0395
0.0897	-0.0591	0.0902	0.0407
0.0997	-0.0622	0.1002	0.0417
0.1197	-0.0676	0.1202	0.0436
0.1396	-0.0718	0.1402	0.0451
0.1596	-0.0750	0.1602	0.0463
0.1796	-0.0769	0.1802	0.0472
0.1996	-0.0778	0.2002	0.0480
0.2496	-0.0762	0.2501	0.0498
0.2996	-0.0732	0.3001	0.0515
0.3496	-0.0692	0.3501	0.0527
0.3996	-0.0645	0.4001	0.0534
0.4496	-0.0590	0.4501	0.0537
0.4996	-0.0526	0.5001	0.0535
0.5497	-0.0454	0.5501	0.0529
0.5997	-0.0373	0.6001	0.0518
0.6497	-0.0285	0.6500	0.0503
0.6997	-0.0188	0.7000	0.0482
0.7498	-0.0083	0.7500	0.0456
0.7998	0.0031	0.8000	0.0438
0.8498	0.0152	0.8500	0.0443
0.8999	0.0282	0.9000	0.0479
0.9199	0.0336	0.9200	0.0502
0.9399	0.0392	0.9400	0.0530
0.9599	0.0449	0.9600	0.0562
0.9799	0.0507	0.9800	0.0599
0.9900	0.0537	0.9900	0.0619
1.0000	0.0567	1.0000	0.0640

Table 2. Single Element Tyrell 026 F1 front wing at reference incidence of 1degree.

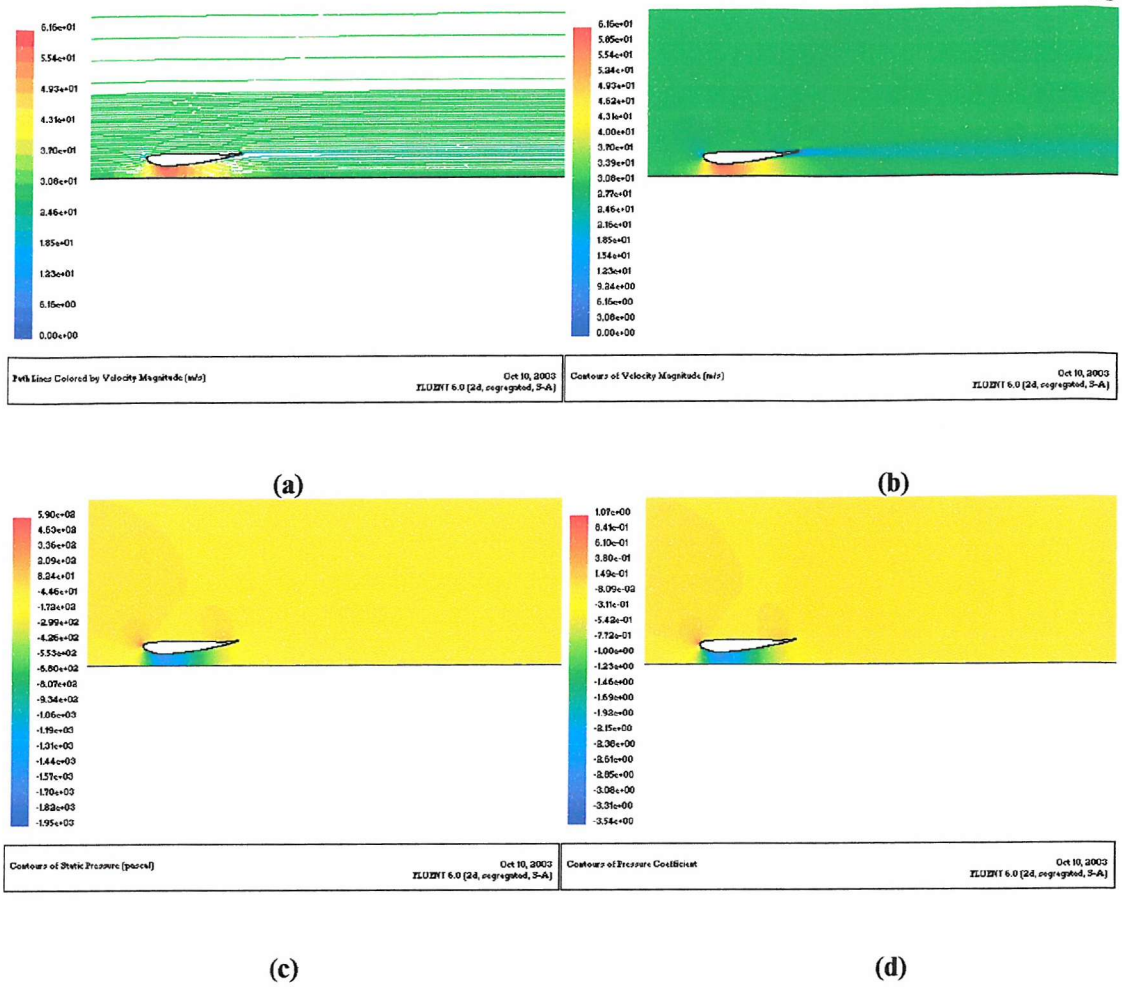

Figure 35. Fluent Results, 30mm Ride Height (a) Velocity Contour Plot; (b) Velocity Flood Plot; (c) Static Pressure Flood Plot; (d) Coefficient of Pressure (C_P) Flood Plot.

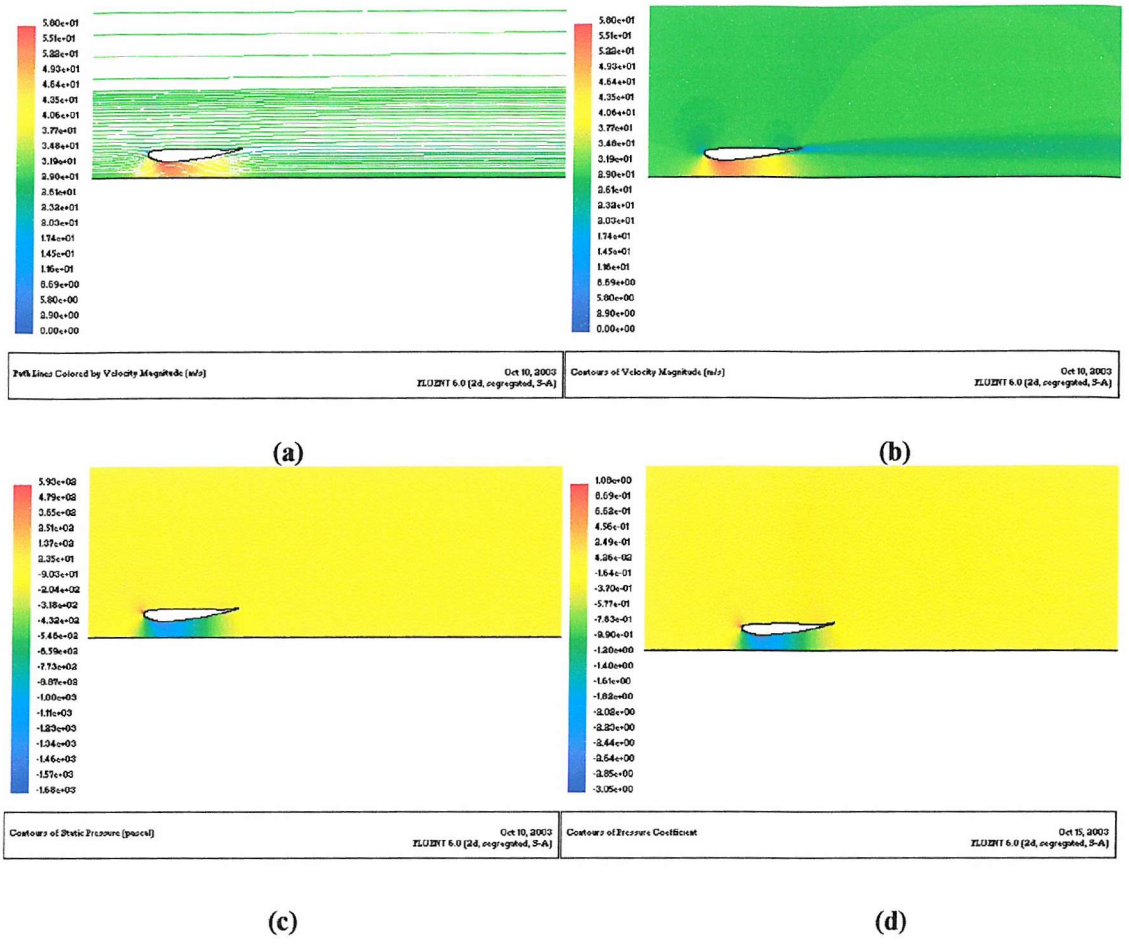

Figure 36. Fluent Results, 40mm Ride Height (a) Velocity Contour Plot; (b) Velocity Flood Plot; (c) Static Pressure Flood Plot; (d) Coefficient of Pressure (C_P) Flood Plot.

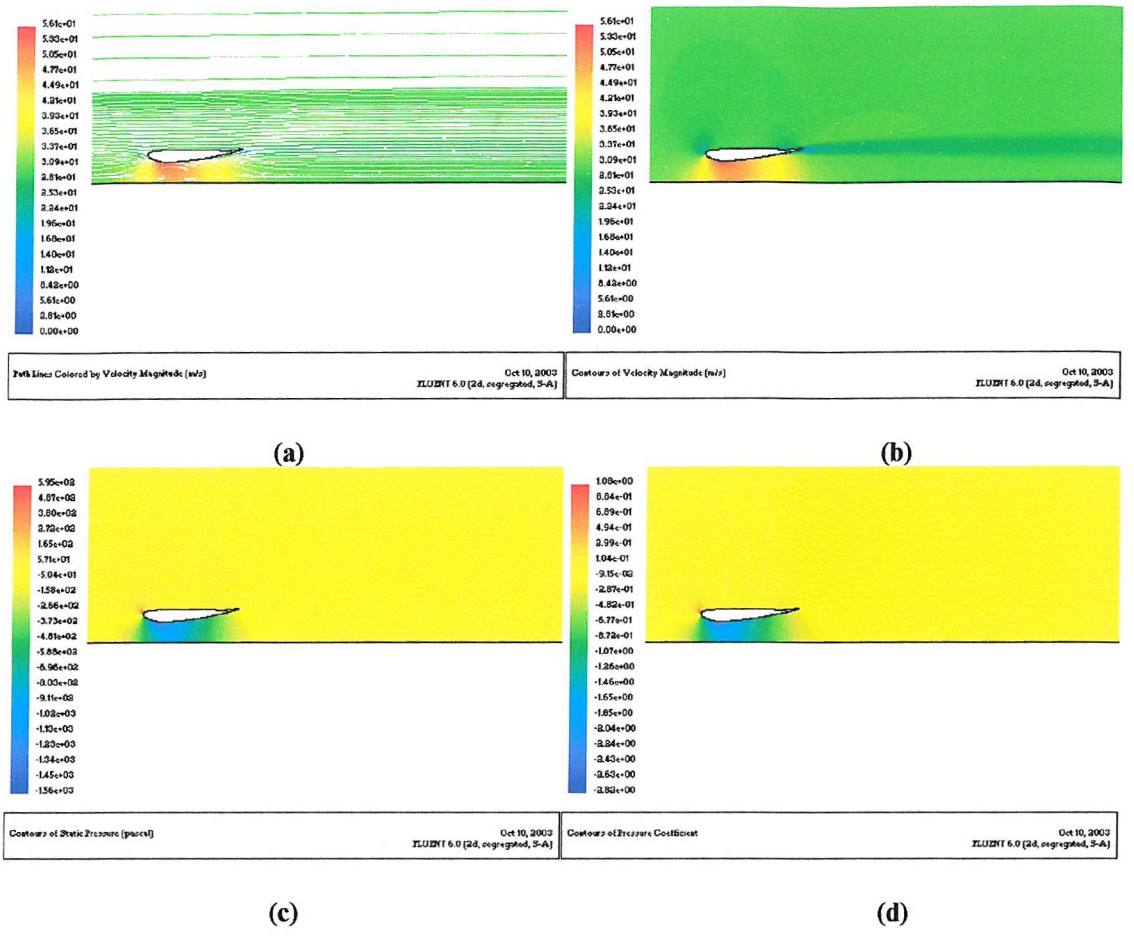

Figure 37. Fluent Results, 50mm Ride Height (a) Velocity Contour Plot; (b) Velocity Flood Plot; (c) Static Pressure Flood Plot; (d) Coefficient of Pressure (C_P) Flood Plot.

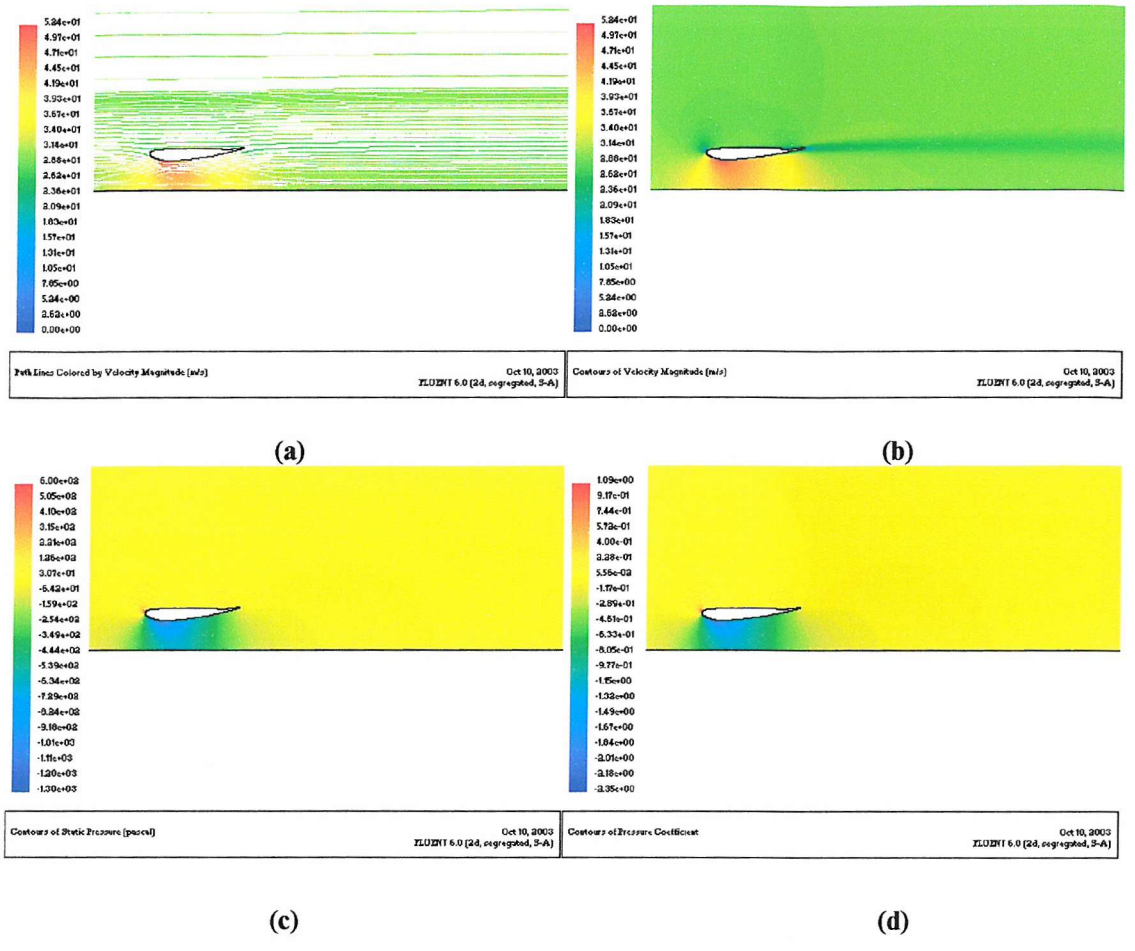

Figure 38. Fluent Results, 70mm Ride Height (a) Velocity Contour Plot; (b) Velocity Flood Plot; (c) Static Pressure Flood Plot; (d) Coefficient of Pressure (C_P) Flood Plot.

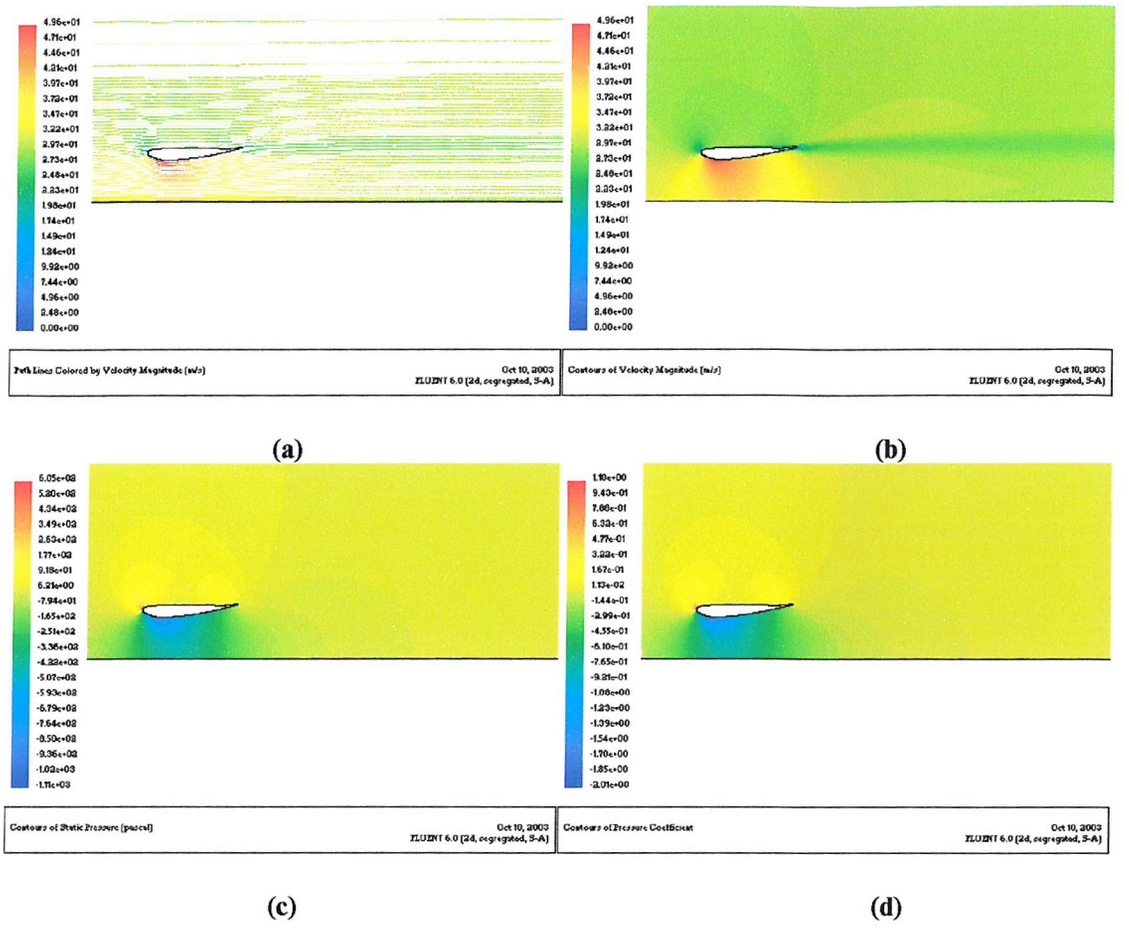

Figure 39. Fluent Results, 100mm Ride Height (a) Velocity Contour Plot; (b) Velocity Flood Plot; (c) Static Pressure Flood Plot; (d) Coefficient of Pressure (C_P) Flood Plot.